Icarus 223 (2013) 775–795

Contents lists available at SciVerse ScienceDirect

Icarus

journal homepage: www.elsevier.com/locate/icarus

Black rain: The burial of the Galilean satellites in irregular satellite debris

William F. Bottke [a,*], David Vokrouhlický [b], David Nesvorný [a], Jeffrey M. Moore [c]

[a] Southwest Research Institute and NASA Lunar Science Institute, 1050 Walnut St., Suite 300, Boulder, CO 80302, USA
[b] Institute of Astronomy, Charles University, Prague, V Holešovičkách 2, 180 00 Prague 8, Czech Republic
[c] NASA Ames Research Center, Space Science Div., MS 245-3, Moffett Field, CA 94035, USA

ARTICLE INFO

Article history:
Received 24 September 2012
Revised 9 January 2013
Accepted 9 January 2013
Available online 30 January 2013

Keywords:
Ganymede
Jupiter, Satellites
Irregular satellites
Callisto
Europa

ABSTRACT

Irregular satellites are dormant comet-like bodies that reside on distant prograde and retrograde orbits around the giant planets. They are likely to be captured objects. Dynamical modeling work indicates they may have been caught during a violent reshuffling of the giant planets ~4 Gy ago (Ga) as described by the so-called Nice model. According to this scenario, giant planet migration scattered tens of Earth masses of comet-like bodies throughout the Solar System, with some comets finding themselves near giant planets experiencing mutual encounters. In these cases, gravitational perturbations between the giant planets were often sufficient to capture the comet-like bodies onto irregular satellite-like orbits via three-body reactions. Modeling work suggests these events led to the capture of on the order of ~0.001 lunar masses of comet-like objects on isotropic orbits around the giant planets. Roughly half of the population was readily lost by interactions with the Kozai resonance. The remaining half found themselves on orbits consistent with the known irregular satellites. From there, the bodies experienced substantial collisional evolution, enough to grind themselves down to their current low-mass states.

Here we explore the fate of the putative irregular satellite debris in the Jupiter system. Pulverized by collisions, we hypothesize that the carbonaceous chondrite-like material was beaten into small enough particles that it could be driven toward Jupiter by Poynting–Robertson (P–R) drag forces. Assuming its mass distribution was dominated by $D > 50$ μm particles, we find that >40% ended up striking the Galilean satellites. The majority were swept up by Callisto, with a factor of 3–4 and 20–30 fewer particles reaching Ganymede and Europa/Io, respectively. Collision evolution models indicate most of this material arrived about 4 Ga, but some is still arriving today. We predict that Callisto, Ganymede, Europa, and Io were buried about 4 Ga by ~120–140 m, 25–30 m, 7–15 m, and 7–8 m of dark debris, respectively. The first two values are consistent with observations of the deepest dark lag deposits found on the most ancient terrains of Callisto and Ganymede. The rest of the debris was likely worked into the crusts of these worlds by geologic and impact processes. This suggests the debris is a plausible source of the dark lag material found in Europa's low-lying crevices. More speculatively, it is conceivable that the accreted dark particles were a significant source of organic material to Europa's subsurface ocean.

© 2013 Elsevier Inc. All rights reserved.

1. Introduction

Jupiter's satellites are often considered to be their own mini Solar System. The largest regular ones by far are the Galilean satellites, Io, Europa, Ganymede, and Callisto, which are comparable in size or larger than our Moon (Fig. 1). They reside near Jupiter's rotation equatorial plane on nearly-circular orbits that are 5.9, 9.4, 15, and 26.4 Jupiter radii from the center of Jupiter, respectively. Their compositions vary as well: Io is largely made of rock, while Europa, Ganymede, and Callisto are composed of ice and rock. The surfaces of the three outermost satellites are dominated by water ice.

If the Galilean satellites are the "planets" of this system, than the irregular satellites are its quasi-Oort cloud. These bodies reside on highly eccentric and inclined orbits (many retrograde) with semimajor axes that are nearly 300 Jupiter radii from Jupiter. The bodies even look like dormant comets, with spectroscopic properties similar to dark C-, D-, and P-type asteroids. For additional description of their properties, see the recent reviews by Jewitt and Haghighipour (2007) and Nicholson et al. (2008).

Along these lines, the proposed origins of the regular and irregular satellites are also different from one another. For example, one scenario suggests that the Galilean satellites formed over the first few My of Solar System history within a gas-starved disk that surrounded Jupiter during its final phase of accretion (e.g., Canup and Ward, 2009; Ogihara and Ida, 2012). The timing of irregular satellite capture, on the other hand, is more poorly understood; it could have been early or as late as several of hundreds of millions of

* Corresponding author.
E-mail address: bottke@boulder.swri.edu (W.F. Bottke).

0019-1035/$ - see front matter © 2013 Elsevier Inc. All rights reserved.
http://dx.doi.org/10.1016/j.icarus.2013.01.008

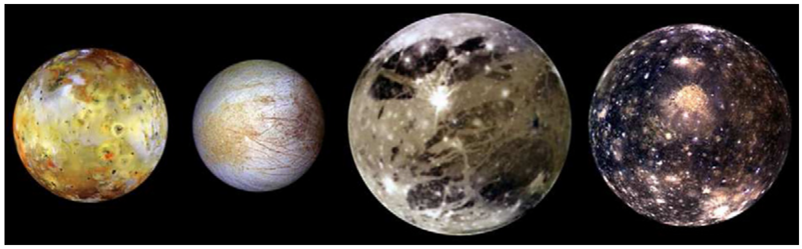

Fig. 1. The Galilean satellites, Io, Europa, Ganymede, and Callisto. They have radii of 1821.6, 1560.8, 2631.2, and 2410.3 km, respectively, and are 5.9, 9.4, 15, and 26.4 Jupiter radii from the center of Jupiter, respectively. Io is a volcanic body dominated by rock, and its surface is very young. The other Galilean moons are composed of rock and ice and have icy surfaces. Their surface ages increase sharply as one moves away from Jupiter. The color differences between these three moons are largely caused by the additional a dark material whose source is unknown. For each world, the regions with the most dark material are also those that are the most heavily cratered. The darkest regions on Ganymede, however, are not as dark as Callisto, even though the spatial density of craters in these regions may be comparable (e.g., Prockter et al., 1998; Schenk et al., 2004). The white spots on Ganymede and Callisto are craters, where bright ice has been dredged up as impact ejecta. This suggests the dark material is mainly a surface veneer. Image credit NASA/JPL/DLR, and courtesy of NASA/JPL-Caltech.

years after this time (e.g., Nesvorný et al., 2007; Bottke et al., 2012). This time gap, if true, could mean there were perhaps few or no irregular satellites present during the formative years of the Galilean satellites. It is also possible early irregulars captured by one mechanism were dynamically removed by a subsequent capture mechanism, say by late encounters between giant planets (Beaugé et al., 2002; Nesvorný et al., 2007). Regardless, this factor, as well as the large distances between the regular and irregular satellite systems, makes it easy to dismiss the irregular satellites as a population that can influence the nature of the Galilean satellites.

Still, there are hints that the irregular satellites have affected the Galilean satellites in some fashion. Consider the following. The mean geometric albedos of Io, Europa, Ganymede, and Callisto are 0.62, 0.68, 0.44, and 0.19, respectively. These values decrease as one moves toward the irregular satellite region (Fig. 1). A closer look at Europa, Ganymede, and Callisto, as shown by a side-by-side comparison (Fig. 2) and high resolution images (Figs. 3–5, respectively), reveal that the dominant darkening agent appears to be deposits of small dark particles. Some of these particles are seen in the crevices of Europa's young surface, while more are seen in the heavily-cratered terrain of Ganymede. At Callisto, nearly all features appear to be blanketed by and/or are mixed with this dark material.

Interestingly, the reflectance spectrum of these terrains appears to be a combination of water–ice and a dark non-icy material that may be similar to carbonaceous chondrites (e.g., Moore et al., 2004; see also McKinnon and Parmentier, 1986). Some have argued that the dark non-icy component on their surfaces, as well as on many other giant planet satellites, appears to be spectroscopically similar to the irregular satellites (e.g., Cruikshank et al., 1983; Buratti and Mosher, 1991, 1995; Buratti et al., 2002; Tosi et al., 2010; Dalton et al., 2012).

This result prompted several groups to suggest that small debris from the irregular satellites might be the source of this material (e.g., Pollack et al., 1978; Johnson et al., 1983; Bell et al., 1985; McCord et al., 1998; see also McKinnon and Parmentier, 1986). We found this to be a highly intriguing scenario, particularly because it has such strong precedents. For example, many authors have suggested links between the small particles driven off of Saturn's moon Phoebe by collisions and the dark leading face of Iapetus (e.g., Soter, 1974; Burns et al., 1996; Verbiscer et al., 2009; Tosi et al., 2010; Tamayo et al., 2011). These particles would evolve inward toward Saturn by Poynting–Robertson (P–R) drag forces (e.g., Burns et al., 1979), with some landing on Iapetus.

To get substantial numbers of small particles, one needs to have two components: a sizable initial population, and lots of collisions. For the latter, we point out that observations of the heavily-cratered surface of Phoebe, its associated dust ring (Verbiscer et al., 2009), as well as the detection of irregular satellite families around many giant planets (e.g., Nesvorný et al., 2003, 2004; see

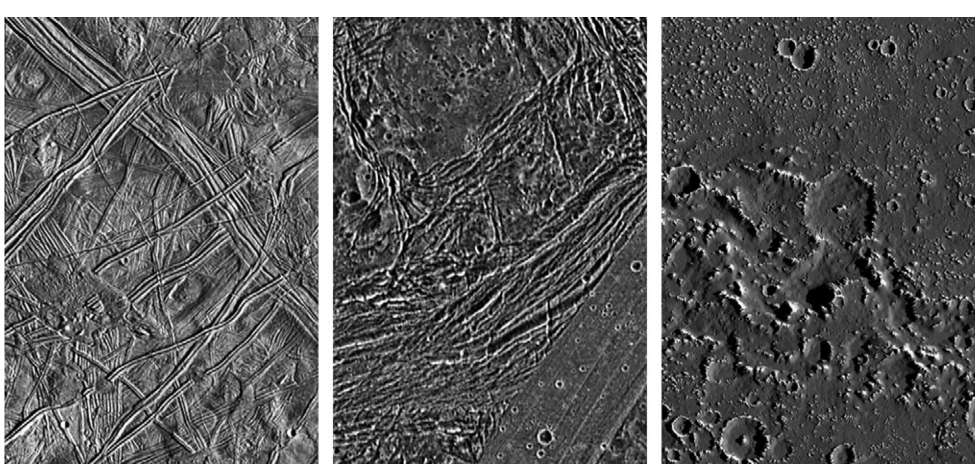

Fig. 2. The surfaces of Europa, Ganymede, and Callisto, scaled to the same resolution of 150 m per pixel. The Europa panel (left) was taken from the region around the Agave and Asterius dark lineaments. It shows few craters and numerous tectonic features. The Ganymede panel (center) was taken from Nicholson Regio. It contains several impact craters and a smaller greater degree of tectonic deformation. The surface is general darker than Europa. The Callisto panel (right) was taken from Asgard basin. It shows numerous impact craters and is covered by a dark layer of material. This layer covers the smaller craters in the image. The most heavily cratered terrains on Ganymede and Callisto are probably close to 4 Gy old, while those are Europa are perhaps less than 100 My old. The images were taken by the Solid State Imaging (SSI) system on NASA's Galileo spacecraft. North is up in all images. The spatial resolution of the original data was 180 m/pixel for Europa and Ganymede and 90 m/pixel for Callisto. Image credit NASA/JPL/DLR, and courtesy of NASA/JPL-Caltech.

Fig. 3. Highest resolution image of Europa's surface, which is centered at 13° south latitude and 235° west longitude. The scale is set so the width is 1.8 km wide. The resolution is 6 m per pixel. The image was taken from an oblique angle, with north to the right of the picture and the Sun illuminating the surface from that direction. Many bright ridges are seen, with dark material concentrated in the low-lying valleys. In the center, the ridges and valleys give way to a darker region of jumbled hills. Small dark, circular features may be impact craters. Image courtesy of NASA/JPL-Caltech.

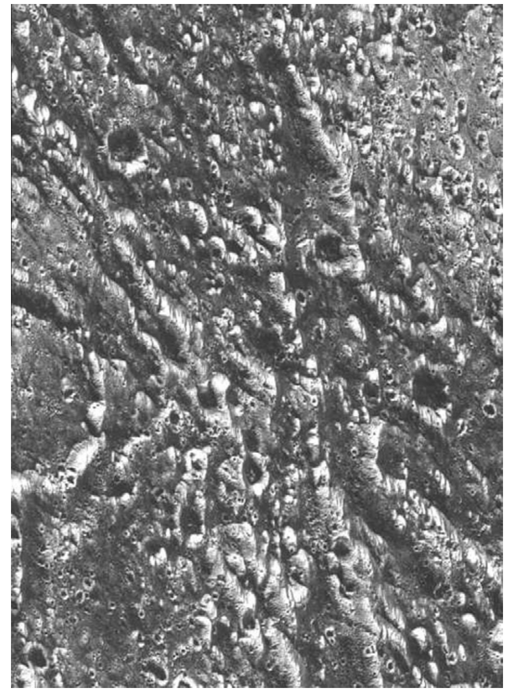

Fig. 4. High resolution images of Ganymede's Galileo Regio region. The scale is 46 by 64 km, with a resolution of 80 m per pixel. The heavily cratered surface is probably many billions of years old and rivals the heavily cratered terrains of Callisto. With that said, the amount of dark material observed here is significantly less than on comparable Callisto terrains (Prockter et al., 1998). The dark and bright lines running from lower right to upper left and from top to bottom are deep furrows in the ancient crust of dirty water ice. North is to the top, and the Sun illuminates the surface from the lower left about 58° above the horizon. Image courtesy of NASA/JPL-Caltech.

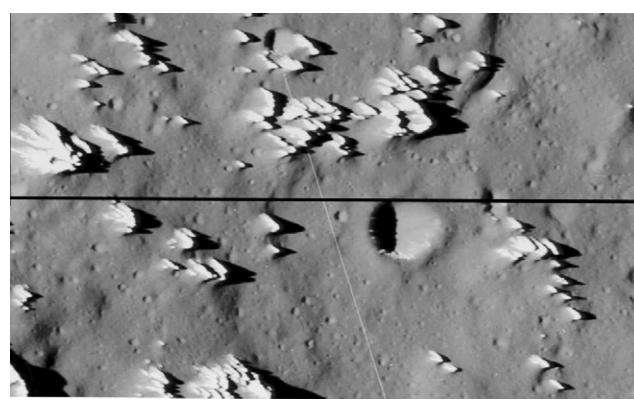

Fig. 5. High resolution images from the region south of Callisto's Asgard impact basin. The knobby terrain contains ice spires with some dark material. As the ice erodes, the dark material apparently slides down and collects in low-lying regions. The knobs are about 80–100 m tall. The smallest features in the images are 3 m across. Dark material blankets the remaining terrain, including the smaller craters. Image courtesy of NASA/JPL-Caltech.

Jewitt and Haghighipour, 2007) all point to collisions being an active process on current irregular satellites. Moreover, the collision probabilities between these bodies tend to be four orders of magnitude higher than those between typical main belt asteroids (Nesvorný et al., 2003, 2004, 2007; Bottke et al., 2010). Thus, if there are irregular satellites, collisions will be a common fact of life.

Beyond this, in Bottke et al. (2010), it was shown that a collisional cascade among a large primordial irregular satellite population could produce enormous amounts of smaller particles, all which would be driven inward toward the central giant planet. In their back of the envelope calculations, they found that this debris, if transferred with high efficiency to Callisto, could potentially produce a deep dark surface layer on the most ancient terrains (e.g., Fig. 5). Moreover, a large quantity of material, if mixed into the upper few kilometers of Callisto's crust by impacts, might explain Callisto's appearance. Any dark dust that gets by Callisto would then have an opportunity to hit Ganymede, potentially explaining its ancient dark terrains as well (see Pappalardo et al., 2004). A catch, however, is that to get sufficient particle numbers, the primordial irregular satellite population would need to have been much more massive in the past. Interestingly, this is actually predicted by the capture scenario of Nesvorný et al. (2007), which we describe in detail below. Thus, many of the key elements needed to put together an end to end model already exist.

This scenario also predicts that dark material on these worlds would be something of a surface veneer. This appears to be broadly consistent with observations. Consider that sizable young impact craters on Callisto often have bright centers and rays, making it appear that they punched through a regolith contaminated by dark material to reach a clean ice zone. Similarly, the most ancient terrains of Ganymede and Callisto, as determined by the spatial density of craters, also happen to be the darkest ones. Conceivably, the amount of dark material present on a given surface might even provide an alternative means to establish a surface age beyond crater counts.

It is notable in Figs. 3–5 that bright icy material tends to be found on the crests of high standing topography, while dark material is mainly found in low-lying areas. This can be readily seen from the highest resolution images of Europa, whose crevices, ridges, cracks, and other low-lying regions often contain a smattering of dark material (Fig. 3). This may suggest mixed-in dark material can be moved by sublimation processes, providing it with some limited degree of mobility once it has been entrained in the icy regolith (e.g., sublimation appears to play an important role in moving ice around on Iapetus; Spencer and Denk, 2010).

All of these tantalizing clues, however, are useless unless we can prove a substantial population of coffee-ground-like irregular satellite particles can reach Europa, Ganymede, and Callisto by P–R drag. Our goal in this paper is to explore this possibility, Accordingly, we use numerically methods to test whether dark material on these worlds may have come from a population of irregular satellites decimated by comminution. Our goal is to calculate the relative flux rates and absolute abundances of dark material that should have reached these worlds. The expressions of dark particles on the saturnian, uranian and neptunian satellite systems will be discussed in future papers (see also Bottke et al., 2010).

The outline of our paper is as follows. After first discussing our irregular satellite capture scenario in greater detail, we develop the dynamical framework for small particle evolution in the Galilean system. We then install this formalism into a numerical integrator and show several proof of concept runs. Next, we perform production runs and discuss the quantity of dark material that can be delivered to each Galilean satellite as a function of particle size. Finally, we discuss our preference for particle size, the likely amounts of material added to each world, and the implications of our work for the Galilean satellites themselves.

Before ending this section, the reader should be aware that we are exploring something of an end-member model in this paper. Our guiding philosophy is to see how far it can go, by itself, in explaining the observed properties of the Galilean satellites. Thus, certain complications, such as the amount of indigenous dark material (IDM) present in the crust and mantles of the satellites after partial/full differentiation, how geologic processes and impact regolith development affect the quantity of a putative fraction of IDM, etc. are not included in our analysis. With this said, we believe we can make an intriguing case that the inclusion of IDM may not be needed to explain observations. Additional discussion of this issue and other model caveats can be found in Section 5.3.

2. A brief history of the irregular satellites

Here we provide additional context for the irregular satellite capture and collisional evolution scenario discussed and used in this paper. Before reading further, however, the reader should consider two points:

- In this paper (and in this section), we follow-up on the implications of the modeling work performed in Nesvorný et al. (2007) and Bottke et al. (2010). We believe these papers provide a coherent story for the evolution of the irregular satellites all the way from their capture to their collisional evolution over the last ~4 Gy. The justification for our starting irregular satellite size distributions can be found in Morbidelli et al. (2009a) and Bottke et al. (2010). At this time, we believe there are no other viable alternative models to test.
- With that said, our modeling work here is largely independent from these works; it mainly requires that one starts with a massive and dynamically-excited irregular satellite population. Thus, as new models come along, their predictions can take advantage of our model results without great difficulty, provided their initial conditions are comparable to those discussed here.

For those readers concentrating on the second point, they can jump ahead to the presentation of our model in Section 3.

There have been numerous scenarios presented in the literature for capturing the irregular satellites. Brief descriptions and references for many can found in Jewitt and Haghighipour (2007) and Nicholson et al. (2008). Nearly all of them, however, have serious issues; we refer the interested reader to Nesvorný et al. (2007) and Vokrouhlický et al. (2008) for details. To claim success, a model not only needs to reproduce the orbits of the observed irregular satellites, which is a major challenge, but it also has to capture the satellites with a high enough efficiency that it can reproduce observations within the context of a plausible outer Solar System evolution model. At present, we argue that the only capture scenario that can fulfill these dual constraints was presented in Nesvorný et al. (2007).

Nesvorný et al. (2007) showed that the irregular satellites were captured during the violent reshuffling of the giant planets as described by the Nice model (Tsiganis et al., 2005; Morbidelli et al., 2005; Gomes et al., 2005). Recall that in the Nice model, the giant planets were assumed to have formed on initially nearly circular, co-planar orbits with a more compact configuration than they have today (all were located between 5 and 12 AU). Slow planetary migration was induced in the jovian planets by gravitational interactions with planetesimals residing in and occasionally leaking out of a $\sim 35 M_{\oplus}$ planetesimal disk between ~15–20 and ~30–40 AU (i.e., known as the primordial trans-neptunian planetesimal disk). These interactions eventually led to a dynamical instability that set all these worlds into motion. Jupiter and Saturn migrated to their current orbits over a timescale of less than a My (Minton and Malhotra, 2009, 2011; Morbidelli et al., 2010), while Uranus and Neptune became unstable and were propelled outward, such that they penetrated the disk and migrated through it. It is even possible that an extra giant planet was thrown out of the Solar System after having repeated encounters with the surviving giant planets (Nesvorný, 2011; Nesvorný and Morbidelli, 2012). This dramatic event scattered the comet-like denizens of the primordial trans-planetary belt population throughout the Solar System.

We find the Nice model compelling because it can quantitatively explain, among other things, the orbits of the jovian planets (Tsiganis et al., 2005; Nesvorný, 2011; Nesvorný and Morbidelli, 2012), the capture of comets from the primordial disk into several different small body reservoirs in the outer Solar System (e.g., Trojans of Jupiter (Morbidelli et al., 2005) and Neptune (Nesvorný and Vokrouhlický, 2009), the Kuiper belt and scattered disk (Levison et al., 2008), and the outer asteroid belt (Levison et al., 2009)). It provides a rationale for the consistency of the magnitude distributions between the Trojans and Kuiper belt, with the Trojans captured from the outer part of the primordial trans-neptunian planetesimal disk (Morbidelli et al., 2009a). Late giant planet migration also drove resonances across the main asteroid belt region from the outside in, which likely triggered the so-called Late Heavy Bombardment (LHB) of the Moon and terrestrial planets (Gomes et al., 2005; Minton and Malhotra, 2009, 2011; Morbidelli et al., 2010; Marchi et al., 2012; Bottke et al., 2012; Morbidelli et al., 2012). These accomplishments are unique among models of Solar System formation.

Note that additional discussion of the viability of the Nice model and so-called Grand Tack model (Walsh et al., 2011) from the perspective of constraints from primitive meteorites can be found in Alexander et al. (2012). The reader should be cautioned, though, that the latest on-line version includes a clarified discussion of several issues compared to what existed in the originally paper published in *Science Express*. In addition, the strongest interpretations of Alexander et al. (2012) rely heavily on D/H measurements of the meteorite Tagish Lake, their assumption that Tagish Lake is representative of material from all D-type asteroids, the D/H ratio of Enceladus, and their interpretation of the nature of Enceledus' formation circumstances.

Nesvorný et al. (2007) realized that many of the comet-like bodies liberated from the primordial trans-planetary belt would be traveling near the giant planets as they were undergoing encounters with one another. Using numerical models, they showed that many of these objects could have been captured during giant planet encounters via gravitational three-body reactions. In other words, the irregular satellites are comet-like objects that just happened to be at the right place at the right time. Intriguingly, these events were capable of capturing on the order of $\sim$0.001 lunar masses of material into isotropic orbits each of the giant planets, much more than we see today. While many of the trapped objects were quickly eliminated by dynamical resonances (e.g., the Kozai resonance; Carruba et al., 2002, 2003; Nesvorný et al., 2003), the remainder were left on orbits that reproduced those of the known irregular satellites. As a byproduct, any putative pre-existing irregular satellites would also be removed. Accordingly, the irregular satellites might be considered first cousins of the Trojan asteroids, Hilda asteroids, scattered disk objects, and P/D-type asteroids in the outer main belt, all which may have originally been members of the primordial trans-planetary disk.

In the original Nesvorný et al. (2007) model, encounters between Jupiter and the other gas giants only took place in a few runs. Subsequent modeling work investigating gas giant systems with five or six planets, however, indicate Jupiter likely had numerous encounters with the gas giants that ended up ejected from the system (Nesvorný, 2011; Nesvorný and Morbidelli, 2012). These encounters would not only permit the capture of numerous comet-like objects, but they would also induce Jupiter to migrate from its starting orbit to its current orbit in <1 My. As a side benefit, this kind of fast, choppy migration reduces the amount of dynamical damage produced to the orbits of the terrestrial planet and main belt asteroids via sweeping resonances, enough to match a myriad of Solar System constraints (Minton and Malhotra, 2009, 2011; Morbidelli et al., 2010; see also Agnor and Lin, 2012).

A potential serious problem with this scenario, however, concerns the observed size–frequency distributions (SFDs) of the irregular satellites. At present, they have extremely shallow power-law slopes for $D > 8$–10 km (Jewitt and Haghighipour, 2007; see Fig. 6) and are limited in mass. Our expectation, however, is that all of these SFDs should really look something like the Jupiter's Trojan asteroid population, whose residents were captured at the same time from the same source population at a roughly comparable efficiency (Morbidelli et al., 2005). An examination shows the Trojans are $\sim$100 times more massive than the irregular satellite population at Jupiter (i.e., on the order of $\sim$0.001 lunar masses) and have a fairly steep SFD, particularly between $100 < D < 200$ km (see Fig. 6). This mismatch is disquieting, and potentially provides evidence that the Nice model is deficient in some manner or even wrong.

A way out of this conundrum is to assume collision evolution has strongly affected the SFD of the irregular satellites. Consider that the mutual collision probabilities between irregular satellites are four orders of magnitude higher than those found among typical main belt asteroids or Jupiter's Trojans (e.g., Bottke et al., 1994, 2010). Combined with impact velocities that are many kilometers per second, it is almost inevitable that robust collisional evolution will place among the irregular satellite populations.

Using the collisional evolution code `Boulder` (see Morbidelli et al., 2009b), and assuming the irregular satellites were captured with Trojan asteroid-like SFDs (Gomes et al., 2005; Nesvorný et al., 2007; Morbidelli et al., 2009a), Bottke et al. (2010) found their model irregular satellite populations literally self-destructed within hundreds of My after capture. A representative sample of their results is shown in Fig. 6. It shows how mutual collisions can readily transform a Trojan-like SFD into Jupiter's irregular satellite SFD. Comparable results were obtained for the irregular satellites at Saturn and Uranus (see also Kennedy and Wyatt, 2011). Bottke et al. (2010) did not treat Neptune because irregular satellite data there is limited, but Kennedy and Wyatt (2011) show a range of reasonable matches can be obtained. Thus, the large-scale demolition of the initial irregular satellite population provides a reasonable way forward for the predictions of the Nice model.

Still, the consequences of this solution lead to a significant follow-up problem, namely determining what happened to the debris produced by all of this collisional evolution. One could simply ignore this issue altogether, given that most fragments are probably too small to be detected from the current generation of telescopes. The difficulty in doing so, however, is that the collisional cascade produced should eventually reduce most of the missing mass into small dark carbonaceous chondrite-like particles. At that point, solar radiation pressure forces and Poynting–Robertson (P–R) drag forces should drive the particles inward toward the central planet (e.g., Burns et al., 1979). Eventually, this material should reach crossing orbits with the outermost regular satellites, with some fraction of this material striking those worlds. These processes have already proven to be the best way to explain the curious bright-dark hemispheric coloration found on Iapetus (e.g., Tosi et al., 2010; Tamayo et al., 2011).

Accordingly, we return to the question asked at the beginning of the paper, namely can we show that Jupiter's irregular satellites have influenced the Galilean satellites in some fashion. We argue here that the answer is yes. As we will show below, Callisto, Ganymede, and to a lesser degree Europa and Io should have been hit and possibly blanketed by dark particles produced by irregular satellite comminution. Given that some of these worlds have not experienced sustained geology or other endogenic processes that can fully hide this material (e.g., Callisto), some of it should still be there. Modeling this scenario also provides us with a set of predictions that can be used to further test the predictions of the Nice model beyond what was done in Nesvorný et al. (2007) and Bottke et al. (2010).

3. Tracking the dynamical evolution of small particles near a giant planet

Here we present our approach to determining the accretion efficiency of small irregular satellite particles striking the satellites of the giant planets. Our formalism is applicable to all of our Solar System's giant planets, so we present the work below in a generic form so it can be readily used by others for future projects.

We assume the particles are released from a zone around a giant planet that was once or currently is populated by irregular

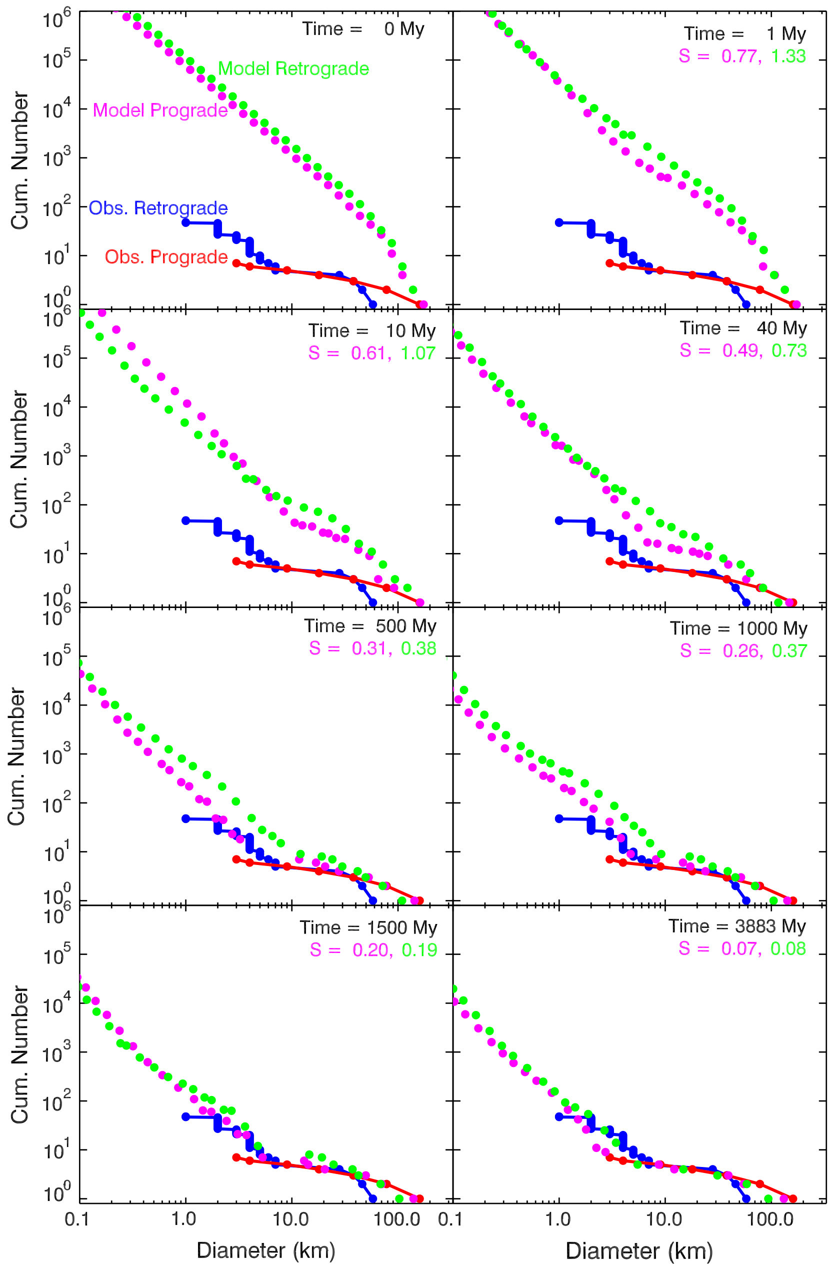

Fig. 6. Snapshots of how Jupiter's initial irregular satellite population undergoes collisional evolution, as computed by Bottke et al. (2010). The starting conditions and collision parameters for their model are defined in that paper. The initial conditions for the run are shown in the time $t = 0$ My panel (top left). The model retrograde and prograde SFDs are represented by green and magenta dots, respectively. They were designed to mimic the shape of Jupiter's known Trojan asteroids. The observed retrograde and prograde SFDs are given by the blue and red dots, respectively. The score S of the prograde and retrograde population at each snapshot time is shown in the legend; $S < 0.3$ is considered an acceptable fit. Our runs show the populations quickly grind away between 40–500 My. Large catastrophic disruption or cratering events often affect the fragment tail for diameter $D < 8$ km objects. The best fit occurs at 3883 My. With no place to go, the carbonaceous chondrite-like fragments are likely ground down to $D < 500$ μm, allowing them to escape toward Jupiter via P–R drag.

satellites (i.e., Fig. 7). For reference, the known irregular satellites of the giant planets have semimajor axes a of ∼0.1–0.5 in units of planetary Hill spheres (R_H), where $R_H = a_p(m_p/(3M_{Sun}))^{1/3}$, m_p is the mass of the planet, and a_p is the planet's semimajor axis from the Sun. The orbits of the particles are affected by the gravitational perturbations of the Sun and regular satellites as well as how the particles react to non-gravitational (radiation) forces. We will show that after a timescale of hundreds of thousands of years (ky) to a few million years (My), most particles are eliminated either by ejection onto heliocentric orbits or by impact onto the giant planet or a satellite.

In the following subsections, we carefully formulate the coordinate systems and modeling tools for the different perturbations. We then present several validity tests in Section 3.5.

3.1. Transformation of coordinates

We start with a minimum system made up of the Sun, a generic gas giant planet (like Jupiter), and its regular satellite system. We assume that particles started from the orbits of the irregular satellites are treated as massless test particles in terms of their effects on Jupiter and the satellites. Into it we introduce an arbitrary

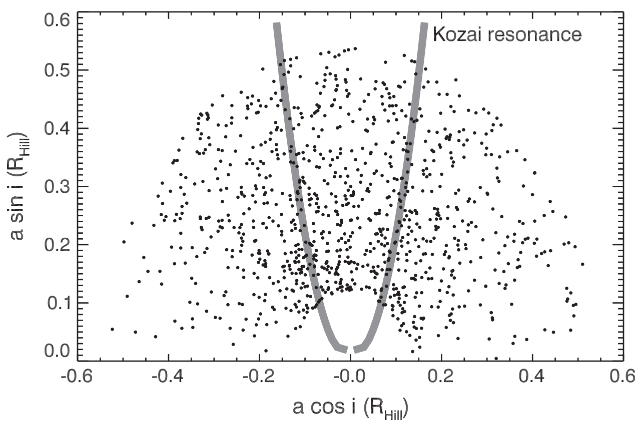

Fig. 7. The initial orbits of our irregular satellite particles. The axes are defined by the planetocentric semimajor axis and the sine and cosine of the particles' inclinations. The particles were initially placed on circumplanetary orbits populating the approximate region where comet-like objects were captured in the model of Nesvorný et al. (2007). Their planetocentric osculating values of semimajor axis were set between $a = (0.04, 0.18)$ AU and eccentricity $e = (0, 0.7)$. These values were scaled by Jupiter's Hill sphere, which is $\sim$0.3552 AU for its mean semimajor axis and $\sim$0.3340 AU when Jupiter is at the pericenter of its orbit with an eccentricity of $\sim$0.06 (roughly the maximum value produced by secular perturbations). We assumed a and e were uniformly distributed in these intervals. The initial orbits were also isotropically distributed in space, with the planetocentric inclination cos$I$ distributed uniformly between -1 and 1. The gray lines correspond to the estimate location of the Kozai resonance in the Jupiter system, according to $\cos^2 i_{\star} = \frac{3}{5}\left[1-\left(1-\frac{R_{\star}}{a}\right)^2\right]$, with $R_{\star}$ the semimajor axis of Callisto (i.e., the outermost satellite capable of efficiently removing the particles). This condition is based on our estimate of a particle's maximum eccentricity during a secular cycle due to solar tides, where the particle is started from an orbit of a given inclination and very small eccentricity (see Nesvorný et al., 2003, as well as comparable calculations in Fig. 8 and Eq. (10) of Carruba et al., 2002). The pericenter distance is then compared to $R_{\star}$. Objects in the Kozai resonance are quickly removed by being driven into Jupiter or by obtaining a high enough eccentricity that they escape into heliocentric space.

inertial system with $\boldsymbol{\rho}_i$ coordinates referenced to its origin: $i = -1$ for Sun, $i = 0$ for the planet, and $i \geqslant 1$ for satellites and massless circumplanetary particles. We then perform a coordinate transformation $[\boldsymbol{\rho}_{-1}, \boldsymbol{\rho}_0, \ldots, \boldsymbol{\rho}_n] \to [\mathbf{T}, \mathbf{R}, \mathbf{r}_1, \mathbf{r}_2, \ldots, \mathbf{r}_n]$ such that

$$\mathbf{T} = \frac{\mu_{-1}\boldsymbol{\rho}_{-1} + \mu\mathbf{t}}{\mu_{-1} + \mu}, \tag{1}$$

$$\mathbf{R} = \mathbf{t} - \boldsymbol{\rho}_{-1}, \tag{2}$$

$$\mathbf{r}_i = \boldsymbol{\rho}_i - \boldsymbol{\rho}_0 \quad (\text{for } i \geqslant 1), \tag{3}$$

where

$$\mathbf{t} = \frac{1}{\mu}\sum_{i\geqslant 0}\mu_i\boldsymbol{\rho}_i, \tag{4}$$

$\mu = \sum_{i\geqslant 0}\mu_i$. Here μ_i denotes gravitational factors Gm_i for each of the bodies in the system (m_i is the mass), while μ is the total gravitational factor of the planet with its satellite system. Thus, $\mathbf{T}$ is the center-of-mass of the whole system, $\mathbf{t}$ is the center-of-mass of the subsystem containing the planet and circumplanetary matter (satellites) and $\mathbf{r}_i$ are planetocentric coordinates of all objects revolving about the planet (satellites and massless particles, e.g., dust particles released in the irregular satellite region). Our parameters are thus a combination of Jacobi-like and relative (planetocentric) coordinates.

The inverse transformation $[\mathbf{T}, \mathbf{R}, \mathbf{r}_1, \mathbf{r}_2, \ldots, \mathbf{r}_n] \to [\boldsymbol{\rho}_{-1}, \boldsymbol{\rho}_0, \ldots, \boldsymbol{\rho}_n]$ reads

$$\boldsymbol{\rho}_{-1} = \mathbf{T} - \frac{\mu}{\mu_{-1} + \mu}\mathbf{R}, \tag{5}$$

$$\boldsymbol{\rho}_0 = \mathbf{T} + \frac{\mu}{\mu_{-1} + \mu}\mathbf{R} - \frac{1}{\mu}\sum_{i\geqslant 1}\mu_i\mathbf{r}_i, \tag{6}$$

$$\boldsymbol{\rho}_i = \mathbf{T} + \frac{\mu}{\mu_{-1} + \mu}\mathbf{R} - \frac{1}{\mu}\sum_{i\geqslant 1}\mu_i\mathbf{r}_i + \mathbf{r}_i \quad (\text{for } i \geqslant 1). \tag{7}$$

We note from (5) and (6) that the heliocentric position vector of the planet is given by

$$\boldsymbol{\Delta}_{0,-1} = \boldsymbol{\rho}_0 - \boldsymbol{\rho}_{-1} = \mathbf{R} - \frac{1}{\mu}\sum_{i\geqslant 1}\mu_i\mathbf{r}_i. \tag{8}$$

3.2. Heliocentric motion of the planet–satellites subsystem

Next, we define the planet and satellites in heliocentric coordinates. Eliminating $\boldsymbol{\rho}_{-1}$ from Eqs. (1) and (2) we obtain

$$\mu_{\rm red}\mathbf{R} = \mu(\mathbf{t} - \mathbf{T}), \tag{9}$$

where $\mu_{\rm red} = \mu_{-1}\mu/(\mu_{-1} + \mu)$. Assuming our system of bodies is isolated, we have $d^2\mathbf{T}/dt^2 = 0$ and thus

$$\mu_{\rm red}\frac{d^2\mathbf{R}}{dt^2} = \mu\frac{d^2\mathbf{t}}{dt^2} = \sum_{i\geqslant 0}\mu_i\frac{d^2\boldsymbol{\rho}_i}{dt^2}. \tag{10}$$

Accelerations in the inertial space are easily given by Newton's gravitational law

$$\frac{d^2\boldsymbol{\rho}_i}{dt^2} = -\sum_{j\neq i}\mu_j\frac{\boldsymbol{\Delta}_{ij}}{\Delta_{ij}^3}, \tag{11}$$

where the summation in j runs over all values $-1, 0, 1, \ldots, n$, $\boldsymbol{\Delta}_{ij} = \boldsymbol{\rho}_i - \boldsymbol{\rho}_j$ and $\Delta_{ij} = |\boldsymbol{\Delta}_{ij}|$. With that we obtain

$$\mu_{\rm red}\frac{d^2\mathbf{R}}{dt^2} = -\sum_{i\geqslant 0}\sum_{j\neq i}\mu_i\mu_j\frac{\boldsymbol{\Delta}_{ij}}{\Delta_{ij}^3}. \tag{12}$$

For particles with $i \geqslant 0$, the sum includes pairs of equal and opposite forces Δ_{ij} and Δ_{ji}, which cancel. The sum therefore reduces to the remaining forces that involve the Sun.

$$\mu_{\rm red}\frac{d^2\mathbf{R}}{dt^2} = -\mu_{-1}\sum_{i\geqslant 0}\mu_i\frac{\boldsymbol{\Delta}_{i,-1}}{\Delta_{i,-1}^3}, \tag{13}$$

$\boldsymbol{\Delta}_{0,-1}$ is given in Eq. (8) and for $i \geqslant 1$ we have $\boldsymbol{\Delta}_{i,-1} = \boldsymbol{\Delta}_{0,-1} + \mathbf{r}_i$. Developing distances to the Sun $\boldsymbol{\Delta}_{i,-1}$ in small differences with respect to the planet–satellites center-of-mass distance $\mathbf{R}$, we obtain

$$\mu_{\rm red}\frac{d^2\mathbf{R}}{dt^2} = -\mu_{-1}\mu\frac{\mathbf{R}}{R^3}[1 + \mathcal{O}(\epsilon)], \tag{14}$$

where the small parameter $\epsilon = \max(\mu_i r_i^2)/(\mu R^2)$.

The value of ϵ from the combined contribution of Ganymede and Callisto at Jupiter is about 4×10^{-10}. It is less for Titan at Saturn, which produces $\epsilon = 2 \times 10^{-10}$, while Uranus and its satellites yield an even smaller ϵ. All of these values are more than an order of magnitude smaller than the fractional error of both solar and planetary gravitational parameters μ. This indicates that the gravitational effects of the satellites minimally affect the heliocentric motion of the planet. Hence, from Eq. (14) we see the elliptical approximation is a sufficiently general solution for the $\mathbf{R}$ vector (see also Section 3.3.3 where we heuristically add effects of the planet–planet perturbations in the time evolution of $\mathbf{R}$).

3.3. Planetocentric motion of the satellites

With $\mathbf{R}(t)$ solved, we turn now to the appropriate description of the satellite's planetocentric motion. Starting with the mass-monopole approximation in (11) we obtain ($i \geqslant 1$ for satellites and/or massless particles)

$$\frac{d^2\mathbf{r}_i}{dt^2}+\frac{\mu_0+\mu_i}{r_i^3}\mathbf{r}_i=-\sum_{j\neq i}\mu_j\left(\frac{\mathbf{r}_i-\mathbf{r}_j}{|\mathbf{r}_i-\mathbf{r}_j|^3}+\frac{\mathbf{r}_j}{r_j^3}\right)-\mu_{-1}\left(\frac{\boldsymbol{\Delta}_{0,-1}+\mathbf{r}_i}{|\boldsymbol{\Delta}_{0,-1}+\mathbf{r}_i|^3}-\frac{\boldsymbol{\Delta}_{0,-1}}{\Delta_{0,-1}^3}\right). \tag{15}$$

The Keplerian planetocentric effect has been moved to the left hand side of (15), while the right hand side contains "perturbations". The first term is the usual satellite–satellite interaction containing both direct and indirect terms. The last term in (15) is the solar tidal acceleration with $\boldsymbol{\Delta}_{0,-1}$ given in Eq. (8). The complete formation of Eq. (15) is used as it is written. The tidal term is often developed in multipole series with quadrupole or octupole truncations, to prevent calculation errors. We did not use this approach, but we have run numerous validation simulations and have carefully examined our production simulations. None so far give any indication that this truncation error ever accumulates to such an extent that it invalidates our results.

In the next several sections, we extended our mass-monopole gravitational formulation with additional effects that are relevant for our work.

3.3.1. Additional effects: planetary oblateness

For our first addition, we included the effects of planetary oblateness. Their gravitational perturbations are small enough that we only included the second and fourth order zonal harmonics in our formulation. The corresponding potential fields in the planetocentric coordinates read (e.g., Bertotti et al., 2003)

$$U_2(\mathbf{r};\mathbf{s})=\frac{1}{2}\frac{\mu_0}{r^3}\left(\frac{R_{\rm pl}}{r}\right)^2 J_2\left[3(\mathbf{s}\cdot\mathbf{r})^2-r^2\right], \tag{16}$$

$$U_4(\mathbf{r};\mathbf{s})=\frac{1}{8}\frac{\mu_0}{r^5}\left(\frac{R_{\rm pl}}{r}\right)^4 J_4\left[35(\mathbf{s}\cdot\mathbf{r})^4-30r^2(\mathbf{s}\cdot\mathbf{r})^2+3r^4\right], \tag{17}$$

where J_2 and J_4 are second and fourth order coefficients of the gravity field, $R_{\rm pl}$ is the associated conventional planetary radius and $\mathbf{s}$ is the unit vector of the planet's rotation axis. Using this notation, the planetocentric equations of motion for satellites and massless test particles should contain the following additional accelerations:

$$\frac{d^2\mathbf{r}_i}{dt^2}=-\left.\frac{\partial U_2(\mathbf{r};\mathbf{s})}{\partial\mathbf{r}}\right|_{\mathbf{r}=\mathbf{r}_i}=\frac{1}{2}\frac{\mu_0}{r_i^5}\left(\frac{R_{\rm pl}}{r_i}\right)^2 J_2\left\{\left[5(\mathbf{s}\cdot\mathbf{r}_i)^2-r_i^2\right]\mathbf{r}_i-2r_i^2(\mathbf{s}\cdot\mathbf{r}_i)\mathbf{s}\right\}, \tag{18}$$

and

$$\frac{d^2\mathbf{r}_i}{dt^2}=-\left.\frac{\partial U_4(\mathbf{r};\mathbf{s})}{\partial\mathbf{r}}\right|_{\mathbf{r}=\mathbf{r}_i}=\frac{5}{8}\frac{\mu_0}{r_i^7}\left(\frac{R_{\rm pl}}{r_i}\right)^4 J_4\left\{3\left[21(\mathbf{s}\cdot\mathbf{r}_i)^4-14r_i^2(\mathbf{s}\cdot\mathbf{r}_i)^2+r_i^4\right]\mathbf{r}_i-4r_i^2(\mathbf{s}\cdot\mathbf{r}_i)\left[7(\mathbf{s}\cdot\mathbf{r}_i)^2-3r_i^2\right]\mathbf{s}\right\}. \tag{19}$$

The ($R_{\rm pl}$,J_2,J_4) constants can be found in the literature for Jupiter or any other planet under consideration. The rotation pole orientation $\mathbf{s}$ should in principle undergo general precession. The relevant timescale is of the order of several hundreds of ky to several My for Jupiter and Saturn, while they are much longer for Uranus. These intervals are comparable to or shorter than the integration timescale for the largest particles used in our simulations.

We have yet to find a handy or reliable analytical representation of the long-term evolution of the pole orientations for our giant planets. For example, the secular representation of the pole motions of Jupiter and Saturn provided in Jacobson (2002, 2007) are only valid over a timescale of several centuries and do not provide satisfactory results over the hundreds of ky to My timescales relevant to our integration lengths. At this time, we choose not to numerically integrate the spin vector $\mathbf{s}$. Instead, we neglect the time dependence in $\mathbf{s}$ and consider the pole coordinates constant.

3.3.2. Additional effects: radiation forces

Radiation forces can strongly affect the dynamical evolution of small particles in the irregular satellite region. We refer the interested reader to several classic papers by Burns et al. (1979) and Mignard (1984) for a general discussion of these effects, with the latter reference concentrating on planetocentric motion (see also Vokrouhlický et al., 2007).

There are two possible sources of radiation that can interact with a particle: (i) the Sun, mainly in optical wavelengths, and (ii) the planet, mainly over thermal wavelengths. While the second source is important for ring particles, it can be neglected in our application for those particles that are far from the planet.

As an useful example, consider the Saturnian system. The solar radiation flux at Saturn's distance from the Sun is $\sim$15 W m^{-2}, while Saturn's thermal flux at the top of its atmosphere is $\sim$4.4 W m^{-2} (e.g., Bertotti et al., 2003). Because the latter component decreases according to $\propto 1/r^2$, where r is distance from Saturn, Saturn's thermal flux at the distance of, say, Rhea, will be $\sim$0.06 W m^{-2}. This is two order of magnitudes lower than the solar flux.

The general formulation of the radiation force, including the first-order velocity dependent component known as the Poynting–Robertson (P–R) effect, can be written as:

$$\frac{d^2\mathbf{r}_i}{dt^2}=\beta\frac{\mu_{-1}}{\Delta_{i,-1}^2}\left[\mathbf{N}\left(1-\frac{\mathbf{N}\cdot\mathbf{V}}{c}\right)-\frac{\mathbf{V}}{c}\right]. \tag{20}$$

See Burns et al. (1979) and Mignard (1984) for details. This acceleration can be added to the right hand side of Eq. (15) for circumplanetary dust particles. Here, $\mathbf{N}=\boldsymbol{\Delta}_{i,-1}/\Delta_{i,-1}$ is the unit position vector of the particle with respect to the radiation source (the Sun) and $\mathbf{V}=d\boldsymbol{\Delta}_{i,-1}/dt$ is its relative velocity with respect to the radiation source (the Sun). Note that the quantity $\boldsymbol{\Delta}_{i,-1}=\boldsymbol{\Delta}_{0,-1}+\mathbf{r}_i$. The β factor, which is the ratio between radiation pressure and the Sun's gravitational pull, is given by $\beta=1.15Q_{\rm sc}/(\rho D)$, where $Q_{\rm D}\simeq 1$, ρ is the bulk density of the particle in cgs units and D is its size in microns (e.g., Burns et al., 1979; Mignard, 1984).

The effect of radiation forces on circumplanetary particles has been extensively studied since the 1980s, with a summary of early work provided by Mignard (1984). In qualitative terms, we can summarize what we know as follows: (i) the direct radiation component produces eccentricity oscillations on the planet's orbital timescale, while (ii) the P–R part, with its drag-like velocity dependence, produces semimajor axis decay toward the planet on the much longer timescale ($\sim 16/\beta$ ky; see text below). Both effects are relevant for the problem of tracking the accretion of small particles onto the regular satellites because both can produce a decrease of the planetocentric pericenter distance.

Interestingly, planetocentric P–R drag produces the semimajor axis decay with $da/dt\propto a$, but it *does not* secularly change the orbital eccentricity of a particle at the same time. This stands in contrast to heliocentric P–R drag, which decreases *both* semimajor axis, according to $da/dt\propto 1/a$, and eccentricity. Consequently, while orbital decay accelerates in the heliocentric case as the particles moves toward the Sun, it actually decelerates in the planetocentric case as the particle moves toward the planet (e.g., Figs. 8 and 9).

Our work here does not account for how the planet's shadow affects the dynamical evolution of a particle (for an analytical treatment of how shadowing modifies ring particle dynamics, see, for example, Vokrouhlický et al., 2007). We neglect this effect because instantaneously changing the radiation force on a particle from a non-zero value in sunlight to zero in shadow can potentially produce spurious results within a numerical integrator. Fortunately, this effect can be neglected in our work; at the distance of Callisto, Jupiter's shadow covers only ⩽1.2% of its orbit, an amount that we consider negligible.

3.3.3. Additional effects: planetary perturbations in R

Up to now, we have assumed the center-of-mass of the planet–satellite system, represented with the **R** vector, moves on a fixed Keplerian orbit about the Sun. In reality, though, planetary perturbations force the orbital elements to change over time. Here we attempt to include these effects into consideration using a simple formulation.

We adopt the following set of non-singular Keplerian elements: $(a, \mathbf{c}_1, \mathbf{c}_2, M)$, where a is the semimajor axis, $\mathbf{c}_1 = (k, h) = e(\cos\varpi, \sin\varpi)$ and $\mathbf{c}_2 = (q, p) = \sin I/2(\cos\Omega, \sin\Omega)$ are non-singular eccentricity and inclination vectors and M is the mean anomaly. The principal secular effects can be represented with a Fourier-like representation of the $\mathbf{c}_1$ and $\mathbf{c}_2$ elements.

We obtained the corresponding frequencies and amplitudes by (i) numerically integrating the planets for 10 My (using DE405 ephemerides initial data at January 1, 2000 for the initial conditions), and (ii) Fourier analyzing the numerically-determined $\mathbf{c}_1$ and $\mathbf{c}_2$ for all of the major planets using the `fmft` code developed by Šidlichovský and Nesvorný (1996). We retained the 25 terms having the largest amplitudes in our analysis; the resulting representation of $\mathbf{c}_1$ and $\mathbf{c}_2$ are very similar to those in Laskar (1988).

3.4. Initial conditions for Jupiter's satellite system

The major planetary parameters and pole positions for Jupiter, Saturn, and Uranus, the gas giants whose irregular satellites were analyzed by Bottke et al. (2010), are provided in Table 1. They were compiled from the literature, mostly from works of R.A. Jacobson and collaborators (e.g., Jacobson, 2000; Seidelmann et al., 2002; Jacobson et al., 2006; Brozović and Jacobson, 2009).

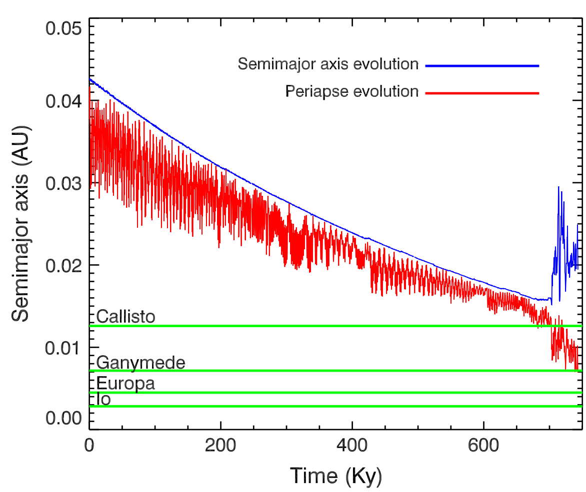

Fig. 8. Orbital evolution of a $D = 50$ μm diameter particle on a prograde orbit in the Jupiter system evolving by P–R drag. Its inclination $i \simeq 40°$. The bulk density of the particle was set to 1 g cm^{-3}. The perijovian distance is shown in red, while the semimajor axis is shown in blue. The green lines show the location of the Galilean satellites. Here we see that the evolution is relatively quiet, with no resonances encountered. Note that unlike P–R drag forces acting on heliocentric particles, (i) eccentricity values for planetocentric particles do not damp, and (ii) the rate at which the semimajor axis decreases slows down near the planet. From here, it reaches an orbit where it encounters Callisto and then goes onto hit Ganymede after 700 ky. Note that the fast oscillations of the eccentricity (and pericenter) due to the Kozai effect are largely under-sampled in this plot; the initial period should be 500 years.

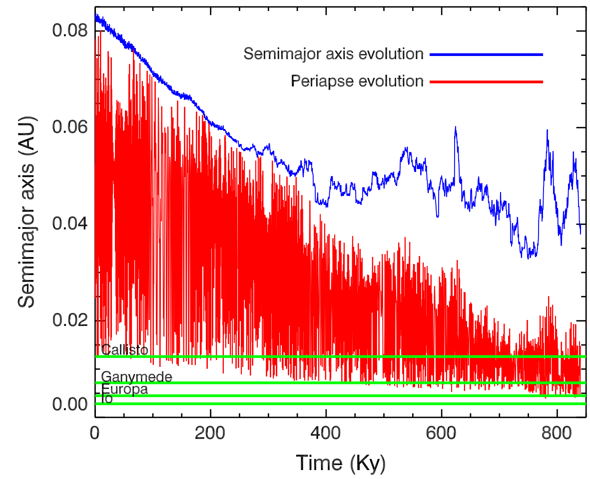

Fig. 9. Orbital evolution of a $D = 50$ μm diameter particle on a retrograde orbit ($i \simeq 125°$) in the Jupiter system evolving by P–R drag. See Fig. 8 for details. During the first ~300 ky, the particle semimajor axis steadily decays due to P–R drag. Then it becomes captured by the Kozai resonance (argument of pericenter oscillates about 90°), which protects the particle from very close encounters with Callisto for another ~200 ky. Note that the pericenter distance is lower than that of Ganymede and Callisto for much of its evolution. The particle eventually impacts Callisto at 841 ky, but not before reaching Europa-crossing orbits. The correlated secular evolution of the eccentricity (and inclination; not shown) is driven by the capture in the Kozai resonance.

The jovian system, as modeled here, has four massive satellites whose orbital planes closely coincide with the orbital plane of the Jupiter about the Sun and also its equatorial plane. For the runs presented below, the initial orbital data for Jupiter's Galilean satellite planetocentric positions and velocities were taken at the January 1, 2000 (MJD51544) epoch from JPL's Horizons system. The key satellite parameters are shown in Table 2. For reference, Io, Europa, Ganymede, and Callisto have radii of 1821.6, 1560.8, 2631.2, and 2410.3 km, respectively. Their semimajor axes around Jupiter are 421,700, 671,034, 1,070,412, and 1,882,709 km, respectively.

3.5. Validation of the integrator and the satellite collision algorithm

The planetocentric coordinates $\mathbf{r}_i$ of the massive satellites and irregular satellite particles, as well as their time derivatives $d\mathbf{r}_i/dt$, which we use in our circumplanetary motion equations, are not canonically conjugated coordinates and momenta. This means we cannot use standard Hamiltonian mechanics/techniques for their description, nor can we easily implement them in numerical procedures such as symplectic integrators. Instead, we decided to use the reliable though slow Burlish–Stoer (BS) integrator for our runs (e.g., Press et al., 2007). After performing several trial runs for the Jupiter system, we adopted 10^{-12} as the intrinsic integration accuracy (see Press et al. (2007) for the proper definition and code-implementation of this parameter). This set the integration timestep to a few hours in length, though for the runs in this paper, the code automatically decreases this value when the particles began to have close encounters with the Galilean satellites or Jupiter itself. This meant that the calculations were extremely computationally expensive.

Next, we tested our scheme by checking the orbital evolution of the Galilean satellites to see if they were in accord with our expectations. In particular, we investigated the time evolution of the critical angle $\varphi = \lambda_I - 3\lambda_E + 2\lambda_G$ of the Laplace resonance in the simulation of the Jupiter system, with λ_I, λ_E and λ_G being the mean longitudes of Io, Europa and Ganymede. Detailed studies of this resonance (indicate that this angle has to liberate about an angle

Table 1
Planetary parameters, with the Jupiter values used in our simulations: μ is the gravitational factor GM, R_{pl} is the assumed radius, (J_2, J_4) are the second and the fourth order zonal coefficients of the gravitational field, and (α, δ) are the pole coordinates, right ascension and declination in the J2000.0 equatorial system. All parameters are given in the AU and day system of units.

Planet	μ	R_{pl}	J_2	J_4	α	δ
Jupiter	2.824760944904983E−7	4.778945025739665E−4	1.4735E−2	−5.888E−4	268.0573	64.4958
Saturn	8.457615150414800E−8	4.028666967091117E−4	1.629071E−2	−9.3583E−4	40.58279	83.53763
Uranus	1.291894847201371E−8	1.751361826139697E−4	3.344E−3	−2.773E−5	77.314	15.175

Table 2
Jupiter satellite parameters used in our simulations: μ is the gravitational factor GM, R_{sat} is the assumed radius, (x, y, z) are the initial components of the planetocentric position vector $\mathbf{r}$ and (v_x, v_y, v_z) are the initial components of the planetocentric velocity vector $d\mathbf{r}/dt$, both at January 1, 2000 epoch (Source JPL/Horizons). All parameters are given in the AU and day system of units.

Satellite	μ x v_x	R_{sat} y v_y	 z v_z
Io	1.328897203998056E−11 2.9941832846650440E−4 9.9253413130177687E−3	1.217664390265676E−5 −2.8093890604131270E−3 1.0829151467297170E−3	 −9.5262059986072652E−5 1.8922945776028900E−4
Europa	7.141226323048062E−12 −4.2252049534454873E−3 −2.5250905174114971E−3	1.043330358106427E−5 1.4550420736581819E−3 −7.5518953307579387E−3	 −2.0339249658295640E−5 −2.4599592253880391E−4
Ganymede	2.204714790644183E−11 −6.9234326850894489E−3 1.6049297762550090E−3	1.758848563717088E−5 −1.8158421301845830E−3 −6.0689875543263353E−3	 −1.4468910600186859E−4 −2.0663632694868140E−4
Callisto	1.600783816213853E−11 4.4518998776038174E−3 −4.4259156139128510E−3	1.611186034177294E−5 1.1737239099998331E−2 1.7150229752440299E−3	 4.4196422133995812E−4 −2.5513299416375682E−6

of 180° with a tiny amplitude of ~0.07° (e.g., Ferraz-Mello, 1979; Peale, 1999).

Looking at the first 100 y of our integrations, we found our estimated libration had the right fundamental period of ~2100 days and an amplitude of ~0.15°. Over much longer time intervals of several My, our data did show an amplitude larger by a factor of few, but the most important factor was that our Io–Europa–Ganymede triple stayed safely locked in their mutual resonance configuration. We found no indication of any disturbances or secular changes. The slight mismatch in our libration amplitude may have to do with some small inaccuracy in our adopted masses or our initial conditions. It might also be some minimal incompleteness of our dynamical model and/or the ecliptic coordinate system used in our integrations. We do not believe these issues affect our results or conclusions in any meaningful way.

Our other verification tests concentrated on the fate of the particles. In principle, our simulations should continue until all of our particles have been removed from the system in some manner. The removal conditions are as follows:

- Impact onto Jupiter, defined as when $r_i < R_{Jup}$, with the latter value being the radius of Jupiter.
- Ejection from the planetary zone of influence, defined as when $r_i > 0.6$ AU. For Jupiter, 0.6 AU is larger than the Hill radius, while long-term stable planetocentric orbits typically only reach to a distance of half of the Hill radius (e.g., Nesvorný et al., 2003).
- Planetocentric semimajor axis smaller than 0.0005 AU. This prevent the particles' orbits from reaching too small an orbital period and thereby forcing us to decrease the integration timestep below a reasonable threshold value of ~0.01 day. Note that these particles can be neglected for our task of deriving the impact probability of irregular satellite particles on Jupiter's Galilean satellites.
- Impact on a Galilean satellite (details provided below).

For our purposes, the most interesting outcome are when the particles strike a satellite. Accordingly, we made a dedicated effort in our runs to identify particle impacts and determine interesting impact parameters.

At each integration timestep, we checked the distance d_i between each particle and the numerically-integrated orbits of the Galilean satellites. If d_i was smaller than the satellite radius R_{sat}, we assumed an impact must have occurred during the last timestep. It is possible, however, that an impact could have occurred in the last timestep with $d_i > R_{sat}$. For that reason, we also stored the positions of all particles and satellites at the previous timestep and then checked whether the connecting line of the previous and current relative position of the particles with respect to the satellites intersect some satellite. If an intersection was found, we assumed a collision had taken place.

When a particle hits a satellite, we compute the exact geometry of the impact itself, namely we determined the angular distance of the impact site with respect to the (i) satellite's apex direction, (ii) the direction to Jupiter, and (iii) the instantaneous direction normal to the orbital plane of the satellite. This information allowed us to determine whether our particles should mainly be swept up on the satellite's apex hemisphere. Ideally, this condition can be compared to predictions from observations. We also extrapolated from the previous timestep, in the satellite's relative coordinates, to see if any particles would hit within the next timestep. This potentially prevented the intermediate timestep of the BS integrator from growing too small for particular impact geometries. In these cases, we again determined the impact site and calculated the output cases (i)–(iii) described above.

We tested our satellite impact algorithm using the following procedures (see below). We selected a satellite and "ejected" a particle from a given surface point. In the reference frame of the satellite, we then moved the particle from tens up to hundreds of satellite radii away from the impact site along the ejection-vector direction, and transformed its position to the planetocentric frame.

Finally, we inverted the velocity of the particle and then used its position and velocity vector as initial conditions for a forward integration test. In general, we found that impacts occurred within a few timesteps if the relative velocity was fast or after a few years if the chosen relative velocity was slow. In each of our tested cases, we were able to reproduce the impact event.

We also directly checked how the timestep decreases when a particle gets close to one of the Galilean (massive) satellites. In particular, we checked that the chosen timestep was linearly dependent on the distance from the satellite when the particle was close; this prevented our code from missing the potential impact on the satellite. It is possible that we may miss some near-grazing impacts, but we do not consider this a serious issue for our results.

Finally, in order to test our satellite impact results, we made comparisons between our production runs below and estimates from an Öpik–Wetherill-like collision code. For this purpose, we used the formulation described by Bottke et al. (1994). This code provided information about the expected number of impacts, though we did not reprogram it to determine the likely directional characteristics of the impacts (i.e., items (i)–(iii) above). We found that our comparisons showed reasonable matches for our tested runs, though the reader should note that it was only designed to work at the order-of-magnitude level.

As an aside, consider that the Öpik–Wetherill method requires the secular angles of the particle-satellite orbits to be fully randomized in the same reference system. In our case, the secular evolution of a particle's orbit is dominated by solar tidal effects, meaning its secular angles circulate in the ecliptic system, while the secular evolution of the satellites' orbits are dominated by planetary flattening and mutual interactions, thereby circulating in the planetary equatorial system. When we account for the tilt of Jupiter's pole and the ecliptic's pole, the satellite nodes do not circulate in the ecliptic system and thus violate the Öpik–Wetherill criteria. At the same time, the influence of the Kozai resonance means that the argument of pericenter for many particles will not be randomly distributed or may have time non-linear evolution (e.g., those trapped in libration with the resonance). These complications are hard to deal without a major investment in code development, so we defined success in these cases to be where the direct integration and Öpik–Wetherill code impact statistics were in the same ballpark as one another. In the future, we will examine whether the modified Öpik–Wetherill code discussed in Vokrouhlický et al. (2012) can provide better results.

4. Results

Using our new code, we explored the orbital evolution of irregular satellite particles in Jupiter's circumplanetary region. All model particles were assumed, for simplicity, to have bulk densities of 1 g/cm^3. They were initially placed on circumplanetary orbits roughly populating the region where comet-like planetesimals had been captured in the model of Nesvorný et al. (2007) (Fig. 7). Our starting orbits corresponded to the planetocentric osculating values of semimajor axis between $a = (0.04, 0.18)$ AU and eccentricity $e = (0, 0.7)$. For simplicity, a and e were assumed to have a uniform distribution in their definition intervals; the orbital distributions of the captured planetesimals in Nesvorný et al. (2007) do not show any obvious trends or a–e correlations. The initial orbits were also assumed to be isotropically distributed in space, with the planetocentric inclination $\cos I$ distributed uniformly between -1 and 1. As will be described in detail below, this means some particles were started on Kozai resonance-stable and Kozai resonance-unstable orbits.

Note that we believe the assumption of an initially isotropic distribution of irregular satellites is a reasonable starting point, but certain dynamical conditions may modify this assumption. Nesvorný et al. (2007) shows that some giant planet encounters favor the capture of prograde or retrograde irregulars; depending on the encounter, we could start with something other than a 50–50% mix. In fact, Bottke et al. (2010) argued the initial distribution of prograde vs. retrograde irregulars in the uranian system was likely to have originally been a 30–70% split. For the Jupiter system, however, the best fits in Bottke et al. (2010) came from runs where the mix was close to 50–50%, our adopted initial conditions.

Beyond this, as time progresses, the somewhat smaller stability zone of the prograde orbits (Nesvorný et al., 2003) may produce an overabundance of retrograde particles. Other effects may also favor retrograde particle collisions (e.g., satellite encounters with retrograde particles tend to produce weaker perturbations). These effects are included in our numerical treatment of particle evolution.

4.1. Individual test particle runs

4.1.1. Standard evolution

Fig. 8 shows the orbital evolution of a 50 μm diameter particle started on a prograde orbit with an inclination of 40° that was initially decoupled from the zone of influence of the regular satellites. The most significant orbital effects found in this simulation are the secular decrease of the planetocentric semimajor axis due to the P–R drag component of radiation pressure and large eccentricity oscillations produced by the combined effects of radiation pressure and solar tides. Note that the short period oscillations of semimajor axis are damped during this evolution: they are most likely caused by solar tidal effects that drop-off with the decreasing distance to Jupiter.

Within its last 30 ky of its life, P–R drag brought the particle within the sphere of influence of the outermost regular satellites, which produced random jumps in semimajor axis via encounters with both Ganymede and Callisto. This eventually led to an impact on Ganymede at time $t \sim 733$ ky. The characteristic timescale of the P–R evolution in this case, where $\beta \simeq 0.023$ (i.e., nominally the ratio of radiation pressure to the gravitational attraction of the Sun on a particle), is $\sim a/(da/dt) \sim 16/\beta \sim 700$ ky (e.g., Mignard, 1984). This value is in good agreement with the observed orbital evolution of the particle.

Callisto and Ganymede, while relatively massive as satellites go, do not have the ability to eject particles out of Jupiter's Hill sphere. This can be easily demonstrated by comparing Jupiter potential energy at Callisto vs. Callisto's potential energy at its surface $(\mu_{Cal}/\mu_{Jup})\,(a_{Cal}/R_{Cal})$; the value obtained, $\leqslant 0.1$, implies that Callisto cannot place enough energy into the particle during a close encounter to eject it out of Jupiter's potential well (e.g., Bertotti et al., 2003; Chapter 18.4). This seals the fate of these kinds of particles; they must always hit a satellite or Jupiter.

It is possible, however, for particles like this one to be ejected during the initial phase of their orbital evolution. Consider particles with high semimajor axes and eccentricities whose orbits are only barely bound to Jupiter. As they evolve by P–R drag, some occasionally reach the Galilean satellites during their perijove passages, where they undergo close encounters. Depending on the encounter, these bodies can reach distances far from Jupiter during apojove ($\geqslant 0.5$ AU), where solar tides can push them out of the system.

4.1.2. Dynamics of the Kozai resonance

Another key aspect of the dynamical evolution of many irregular satellite particles involves the Kozai resonance (sometimes called the Kozai instability). Consider that immediately after being captured, the irregular satellites probably comprise a isotropic distribution of impactors within Jupiter's Hill sphere with a between 0.04 and 0.18 AU (Fig. 7; see also Nesvorný et al., 2007). The zones with inclination i values between $60° < i < 130°$, however, are in the Kozai resonance, and are readily pushed into the Galilean satellite region (Carruba et al., 2002, 2003; Nesvorný et al., 2003). This does allow these objects to potentially hit the Galilean satellites, but time is not on their side; most are quickly eliminated by striking Jupiter or by being ejected from the jovian system.

In the production runs described below, we typically find that ~50% of our starting particles are removed from our simulation within a few hundreds to a few thousands of years. This Kozai timescale corresponds to $\sim P_{\rm p}^2/P_{\rm s}$, where $P_{\rm p}$ is the orbital period of the planet's heliocentric motion and $P_{\rm s}$ is the orbital period of the satellite's planetocentric motion (e.g., Carruba et al., 2002, 2003; Nesvorný et al., 2003). At Jupiter, where $P_{\rm p} \sim 10$ y and $P_{\rm s} \sim 1$ y, it only takes a few hundreds of years to eliminate most particles from the Kozai instability zone. The effects of radiation pressure can even accelerate this process by boosting planetocentric eccentricity values (e.g., Hamilton and Krivov, 1996).

Our numerical results correspond well to the behavior seen in Fig. 5 of Nesvorný et al. (2003). Thus, when we express the fraction of starting particles accreted onto the regular satellites, we also specify the reference population of particles, namely the total fraction of captured bodies or those that survive the first few Kozai cycles.

The Kozai resonance, however, can also produce unexpected effects. In Fig. 9, we started a 50 μm diameter particle on a retrograde orbit with an inclination of 125° close to the Kozai zone. Inward migration allowed it to be captured in the Kozai resonance, circulating about a stable point in the e–ω plane, where e is eccentricity and ω is the argument of pericenter. This motion protects both eccentricity and inclination from large oscillations and keeps ω oscillating about the 90° value. This helps the particle to survive longer because its orbit intersects the orbital plane of the Galilean satellites at a true anomaly value of ~±90° (i.e., at a distance $\sim a(1-e^2)$ larger than the pericenter distance $q = a(1-e)$). The same protection mechanism that works here helps Pluto and many plutinos avoid close encounters with Neptune (Milani et al., 1989). Still, the protection is not complete, with sudden jumps in the particle's semimajor axis suggesting close encounters do happen from time to time.

These Kozai protection mechanisms can delay some particles from hitting the Galilean satellites, or may allow them to evolve onto orbits where they can hit a number of satellites. Overall, we find that about 10% of our particles "park" themselves in these Kozai-protected states. Many particles also enter into protective capture orbits as a consequence of semimajor axis evolution driven by P–R drag.

4.1.3. Comparing collision rates for prograde and retrograde particles

Highly eccentric particles also have interesting collision outcomes. These bodies spend little time near pericenter where they can interact with the Galilean satellites, so their collision rates may be longer than one would expect for satellite-crossing bodies. The timescale for a collision can be estimated using $\sim 1/\left(P_i R_{\rm sat}^2\right)$, where P_i is the Öpik–Wetherill-like intrinsic collision probability. For a particle orbit with $a \simeq 0.09$ AU, $e \simeq 0.9$ and $I \simeq 130°$, we obtain an mean collision interval of ~430 ky for hitting Callisto. This is in a rough agreement with our simulation results. If we were to consider a prograde particle with $I \simeq 50°$, we would obtain an estimate for the accretion timescale $\sim 1/\left(P_i R_{\rm sat}^2\right) \sim 730$ ky for hitting Callisto.

A broader point to make here is that retrograde particles have higher collision probabilities with the Galilean satellites than prograde ones. This is because their synodic period of relative motion with respect to the satellites is shorter and thus in a given interval of time they may encounter the satellites more frequently. The impact velocity for the retrograde particle is also higher: for the example above, the retrograde vs. prograde impact velocities on Callisto are ~17.5 km/s vs. 9.7 km/s, respectively.

An examination of many different particle orbits shows that prograde particles on highly eccentric orbits are generally more perturbed by satellite close approaches than retrograde ones and thus are more vulnerable to ejection. This is reflected in our production results, where retrograde orbits are generally found to be more stable (long-lived) over longer time periods than prograde particles. As an aside, this result can be understood from the fact that in the patched conic approximation, the change in a particle's velocity in a close encounter can be expressed as a function of the ratio of the particle's relative encounter velocity to the satellite's escape speed, and that prograde particles have a lower relative velocity. Note that our results may also be compounded by the numerical result that solar tides produce a larger zone of stability for retrograde satellites than prograde ones (e.g., Nesvorný et al., 2003).

4.2. Production runs

For our production runs, we started thousands of particles on isotropic circumplanetary orbits as defined in the beginning of this section (see also Fig. 7). These values allowed us to obtain reasonably robust impact statistics on the satellites. The diameters of our particles were $D = 5$ μm, 10 μm, 20 μm, 50 μm, 100 μm and 200 μm. Their initial orbits were randomly chosen over a set of planetocentric osculating elements in semimajor axis a, eccentricity e, and inclination i as described above. The other orbital angles (longitude of ascending node Ω, argument of periapse ω, mean anomaly M) were chosen at random between zero and 360°. The accretion efficiency of these particles onto Io, Europa, Ganymede, and Callisto are both listed in Table 3 and are shown in Fig. 10.

As a caveat, we note that our results do not include electromagnetic forces, which should become increasingly important for $D < 20$ μm particles approaching the vicinity of Jupiter (e.g., Burns et al., 2001). We do not believe the exclusion of these forces from our model has affected our impact statistics, partly because the Galiean satellites are relatively far from Jupiter but also because we have restricted our model results to $D > 5$ μm particles. Nevertheless, these effects should included if any reader attempts to extend our model to very small particles or small- to middle-sized particles hitting objects inside the orbit of Io.

We find that approximately half of the particles are readily eliminated within the first ~10–20 ky due to the Kozai instability. Most of these bodies have little opportunity to collide with the regular satellites because their dynamical lifetimes are much shorter than their characteristic collision timescales (see Section 4.1.2 above). This sets an upper limit on the fraction of material that can potentially hit the Galilean satellites under our initial conditions.

The accretion rate on the Galilean satellites is a function of several factors: (i) the P–R drift speed of the particles, with smaller particles migrating more quickly than larger ones, (ii) the size of the satellites, with the largest ones on the outside (i.e., recall that the satellite diameters of Ganymede and Callisto are much larger than Io and Europa; Table 2 and Section 3.4), (iii) the orbital speed of the satellites, with the fastest speeds for those closest to Jupiter, and (iv) the attrition rate of the particles as they move inward, with Callisto getting the first chance to accrete the particles, then Ganymede, and so on. Our numerical simulations suggests these factors combine to produce accretion trends that essentially match our expectations.

In general, larger, slower-moving particles, defined here as those with $D \geqslant 50$ μm, are the most likely to be swept up by the outermost moons. This explains why Callisto accretes the largest fraction of all of the particles, with next-in-line Ganymede coming

Table 3
Accretion results of irregular satellite particles onto the Galilean satellites. We examined particles of diameter 5 μm, 10 μm, 20 μm, 50 μm, 100 μm and 200 μm. These objects were tracked until their demise, with impacts recorded on the four Galilean satellites (Io, Europa, Ganymede and Callisto). The number of recorded impacts on the respective satellite is given in the table. The last two rows give additional diagnostic about the run: "Total impacts" is the total number of impacts on all regular satellites, and "Total TPs init" is the initial number of particles in the simulation.

Satellite	5 μm	10 μm	20 μm	50 μm	100 μm	200 μm
Io	29	41	52	34	39	21
Europa	21	40	72	51	37	16
Ganymede	49	156	305	274	279	155
Callisto	33	208	590	917	936	670
Total impacts	132	445	1019	1276	1291	862
Total TPs init	5000	3000	3000	3000	3000	2000

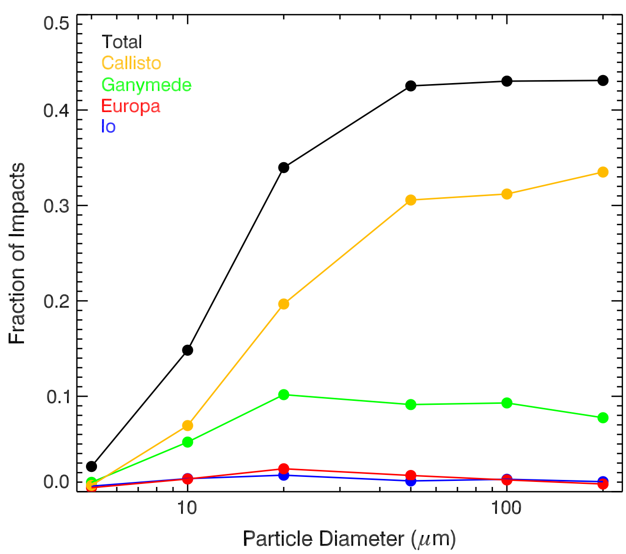

Fig. 10. The efficiency of irregular satellite particle accretion on the Galilean satellites. Thousands of particles with $D = 5$, 10, 20, 50, 100, and 200 μm were initially released from the irregular satellite zone (Table 3). They evolved inward by both gravitational and non-gravitational P–R forces. The black curve shows the net fraction of accreted particles striking the Galilean satellites. The blue, red, green, and gold curves show the fraction of the particles that hit Io, Europa, Ganymede, and Callisto. Nearly half of all particles are lost by being placed within the Kozai resonance at high inclinations. Of they remaining half, the largest fraction strike Callisto, the outermost moon, and then Ganymede. The accretion efficiency increases for large particles because they migrate toward Jupiter much more slowly than smaller ones, thereby giving the particles a better chance to hit a satellite.

in second. Overall, about 43% of all slow-moving particles end up hitting at least one of the Galilean satellites, with a third going to Callisto and ~10% to Ganymede (Fig. 10). Relatively few of the large particles get to Io and Europa.

Small particles, such as those that are $D < 10$ μm, have orbits that decay fast enough by P–R drag that they can largely bypass the Galilean satellites on their way to hitting Jupiter. As a consequence, only a small fraction hit the satellites (3% for 5 μm particles), but they do so fairly uniformly over all of the satellites. Here the accretion advantages of the outer satellites (i.e., larger sizes; first opportunity to accrete particles) are compensated somewhat by the higher orbital speeds of the inner satellites. As we move to larger particles ($D > 20$ μm), the P–R drift rates slow significantly, enough to allow most of the available non-Kozai particles to accrete on the outermost satellites.

The timescales for the particles to hit the Galilean satellites are shown as a function of osculating inclination in Fig. 11. To interpret these results, it is useful to consider three timescales.

(1) The first and fastest timescale corresponds to those bodies in the Kozai instability. Those particles near $i \sim 90°$ undergo large e oscillations over hundreds of years, with peak values high enough to drive them into Jupiter. This short interval dominates the other timescales below, and allows the Kozai instability to produce the intermediate-i gaps seen in Fig. 11.
(2) There is semimajor axis decay from P–R drag, whose timescale is $\propto 1/D$. This dependence on particle size is readily seen in Fig. 11, with the mean impact timescale increasing with increasing diameter. More quantitatively, consider that the 50% accretion values for 20 μm particles are between 100–400 ky for Callisto, while those for 100 μm particles are 1.5 My.
(3) The collision timescale is the average time it takes for a particle to hit a satellite once it reaches a crossing orbit with a (typically) high-e orbit. For particles crossing Callisto's orbit, this timescale is often of the order of 500–700 ky. As discussed in Section 4.1.3, these timescales can also be extended by high eccentricities among the particles; recall that planetocentic P–R drag does not decrease e.

In terms of Fig. 11, the second timescale dominates the $D < 20$ μm particles and keeps their overall accretion values low. For the $D > 50$ μm particles, the P–R drag timescale is slow enough that the third timescale dominates. In terms of accretion, this allows Callisto to accrete the most particles for nearly all inclination values. Those particles that do manage to hit the inner moons often have certain characteristics. A few with high e values simply wait for P–R drag and satellite encounters to drop their a values enough for them to reach crossing-orbits with the inner moons. Others have starting inclinations near the Kozai zone and have their e values rapidly increased to inner satellite-crossing orbits by solar perturbations.

Interestingly, the "excluded Kozai range" gets broader in Fig. 11 as particle size decreases. This is because the smaller particles get increasingly larger-amplitude eccentricity oscillations from radiation pressure and therefore do not need such a high initial inclination to hit the Galilean satellites. The curious fact that there is not an excluded Kozai range for $D = 5$ μm particles is due to radiation pressure, which gets strong enough near that size to interfere with the pericenter motion and suppress Kozai cycles. This effect is described in more detail in Tamayo et al. (2013).

The directional characteristics of our impacts onto the Galilean satellites are shown in Fig. 12. Here we plot the cumulative probability distribution of the cosine of the angle between the impact site and the apex direction of the satellite. We define this angle as α. The $\cos\alpha$ values are plotted for our 10 μm and 100 μm diameter particle runs (see Table 3). We have also tracked the angles between the impact site and the radial direction to the planet as well as the normal direction to the orbital plane of the satellite. These angles tend to be uniformly distributed. In general, $\cos\alpha$ is strongly skewed toward the apex direction. This means that majority of the particles should land near the apex hemisphere on all of the Galilean satellites. This feature is no surprise, and is readily explained by the sweeping effect of satellite motion in an otherwise isotropic cloud of particles around the planet.

Our results tend to match our intuition, namely that after an initial clearing phase, when close to half of the particles in the population are lost, the remaining particles slowly migrate toward the planet by P–R drag and are brought deeper and deeper in the gravitational well of Jupiter. Recall that the rate da/dt due to the P–R drag is proportional to a and thus the decay stalls out close to the planet. When the semimajor axis of a particle is small enough, satellite encounters lack the ability to eject them outside of Jupiter's Hill sphere. At that point, they generally impact one of the satellites unless they can reach Jupiter first.

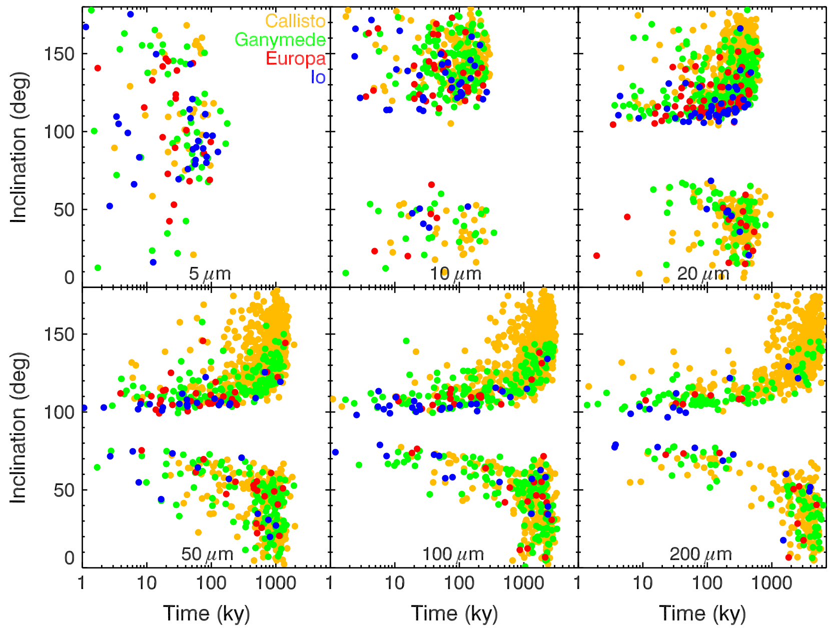

Fig. 11. The accretion timescale of irregular satellite impacts on the Galilean satellites as a function of the particles' initial osculating inclinations. The blue, red, green, and gold dots show correspond to impacts on Io, Europa, Ganymede, and Callisto. The particle diameter is given at the bottom of each frame. The earliest impacts correspond to those bodies in or near the Kozai instability, located at inclinations near $i \sim 90°$. The time to hit a satellite increases with increasing particle size because P–R drag is less effective at semimajor axis decay. Retrograde particles have higher collision probabilities with the satellites, so in general they are much more likely to hit the outermost moons than prograde particles, at least until P–R drag becomes very slow. Note that the largest particles can strike the innermost moons if they start near the Kozai resonance.

5. Dark particle deposition on the Galilean satellites

Here we summarize what we have learned about particle deposition on the Galilean satellites:

- *Impact efficiency.* Impacts on the Galilean satellites, as determined by our simulations, are fairly numerous for large particles. For $D > 20$ μm particles initial placed on isotropic orbits far from Jupiter, between 34% and 43% end up striking one of the Galilean satellites.

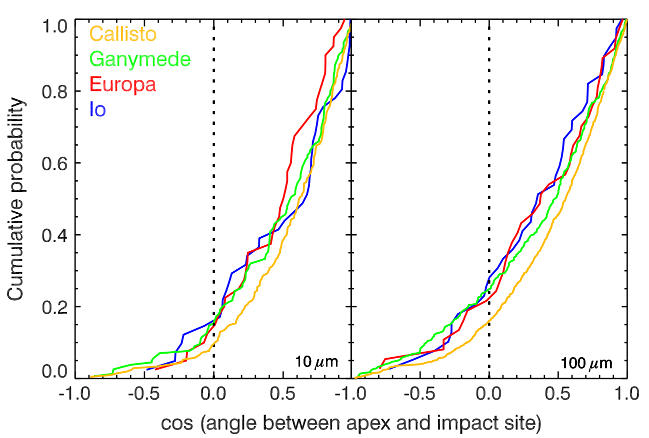

Fig. 12. Cumulative probability distribution of the $\cos\alpha$ parameter for 10 μm (left) and 100 μm (right) diameter particles striking the Galilean satellites, where α represents the angular distance from the apex (leading) direction. The blue, red, green, and gold curves correspond to impacts on Io, Europa, Ganymede, and Callisto. For both sets of runs shown here, we find the α has a preference for impacts toward the apex hemisphere (i.e., $\cos\alpha > 0$). For inert satellites in synchronous rotation, this effect should produce a build up of dark material on their leading hemisphere. The fact that this effect is not obvious from observations (e.g., Fig. 1) could suggest that the satellites have extremely young surfaces (Io) or that they experience non-synchronous rotation (Europa, Ganymede, Callisto).

- *Impact progression.* Most of our large particle impacts are on Callisto and Ganymede, the outermost Galilean satellites. This is readily explained by the dynamical evolution of the dust grains, whose slow inward transport inward by P–R drag means that few can drift past both of these large worlds.
- *Impact sites.* Many more particles hit the apex hemisphere than the antapex hemisphere. This is readily explained by satellite motion through an isotropic cloud of particles.

Using our data and these ideas, we can now estimate the approximate thickness of dark material added to each of the Galilean satellites over time. This will be accomplished by combining our accretion efficiency results (Table 3; Fig. 10) with estimates of how much mass loss should have taken place among Jupiter's irregular satellite population since they were captured (assumed to be about 4 Gy ago; see Bottke et al. (2012) and Morbidelli et al. (2012) for a discussion of how this value was chosen).

5.1. Calculation assumptions

For our collision results, we apply a set of outcomes taken from Bottke et al. (2010), who modeled collisional evolution among the irregular satellites and reproduce the observed populations. In their work, objects ground down to $D < 0.1$ km were placed into a "trash bin", where it was assumed they would be readily beaten into small enough particles that P–R drag could take them into the Galilean satellite region. Additional assumptions related to this run and the population itself can be found in Bottke et al. (2010).

Our calculations make several additional assumptions. First, we limited our analysis to the Bottke et al. run shown in their Fig. 7, which is our Fig. 6. We believe this is warranted because most of the best fit cases for Bottke et al. (2010) produce evolutionary results that are fairly similar to one another. The major difference between their best fit runs comes from (i) the starting mass of the stable irregular satellite population and (ii) the nature and timing of cratering and disruption events. In Fig. 6, we assumed a starting mass of 0.0008 lunar masses for our stable population placed into $D > 0.1$ km objects, with the bulk density of each object set to 1 g cm^{-3}. Other reasonable fits were found by Bottke et al. (2010) for starting populations that were 3–30 times larger than the one used here. Larger starting masses translate into deeper particle depths on the regular satellites. It is unclear that these larger populations are needed to match the constraints discussed below, but they could potentially provide margin against any unforeseen dark particle loss mechanisms.

Second, the Galilean satellites are assumed, for the moment, to be inert spheres. This allows them to preserve all of the dark material that lands on them. In reality, an unknown fraction of the dark material landing on Europa, Ganymede, and Callisto should be mixed into the icy regolith of each world by impact events, sublimation, and geologic processes. Another unknown fraction should hit, fragment, and possibly vaporize, though most of the solids should be left behind (see, for example, Artemieva and Shuvalov, 2008). These issues are not treated here, but they are discussed in greater detail in Section 5.3.

Third, given our model's preference for dark dust impacts near the apex for each world (Fig. 12), our calculations implicitly assume that the Galilean satellites have experienced non-synchronous rotation (NSR). We believe this is a reasonable approximation for several reasons. The enormous moons Europa, Ganymede, and Callisto, as well as Saturn's moon Titan, are all thought to have subsurface oceans beneath their icy interiors (Khurana et al., 1998; Kivelson et al., 1999, 2000, 2002; Pappalardo et al., 1999; Schubert et al., 2004). This is likely driven by obliquity forcing from planetary tides, which appears capable of dissipating enough heat in Europa, Ganymede, Callisto, and Titan to maintain their oceans over billions of years (Tyler, 2008; see also Bills, 2009). In general, oceans should make it easier for the interiors and exteriors of these icy worlds to decouple from one another and/or to undergo true polar wander (e.g., Zahnle et al., 1998; Mohit et al., 2012).

Related lines of evidence for NSR among these ocean moons are as follows:

- The orientation of its strike-slip faults and cycloids on Europa are consistent with an icy shell that has experienced recent episodes of NSRs (see Rhoden et al. (2012) and references therein).
- The expected apex–antapex asymmetry in crater density for Ganymede is far weaker than that predicted by cratering models; models predict an apex–antapex disparity on Ganymede of 15–40 times, while the observed difference is only 4 (Zahnle et al., 2001; Schenk et al., 2004; Dones et al., 2009). Crater chains are also seen to be scattered across Ganymede, while models would predict the should be concentrated on the side facing Jupiter (Zahnle et al., 2001; Schenk et al., 2004). Finally, the leading hemisphere is brighter than the trailing hemisphere.
- No crater asymmetry is observed on Callisto, while models suggest a difference of at least an order of magnitude (Zahnle et al., 2001). Crater saturation could play a role in erasing this difference, but there are reasons to be skeptical that it matters very much for the larger crater sizes.
- The rotation rate of Titan, as derived from radar experiments, is not constant over a period of several years, with surface features possibly shifting by 0.36° per year in apparent longitude (Lorenz et al., 2008). We caution, though, that this data is currently being reanalyzed, with the latest results perhaps only suggesting weak evidence for NSR.

With this said, there is also evidence for hemispheric differences between the leading and trailing hemispheres on Callisto that has been attributed to exogenic dust (Buratti, 1991; Bell, 1984). In fact, Callisto's trailing side appears to be 12% brighter than the leading side. This interpretation is complicated, though, with the best data on this issue coming from groundbased photometry taken during the 1970's (e.g., Morrison and Morrison, 1977). If we take this measurement at face value, it suggests a pattern that is the opposite of what is seen on the other Galilean satellites. This is a strange result unless NSR is common among these worlds; Callisto in synchronous rotation would presumably have a dark leading hemisphere. On the other hand, high speed collisions at the apex of a synchronously rotating Callisto might plausibly alter the scattering properties and micro-structure of the surface.

Regardless, we caution against over-interpreting the data, particularly when it limited. For example, a possible way we could miss the apex/antapex difference would be if there is so much dark dust deposition on Callisto that the leading/trailing hemispheres were both buried to a depth greater than the detection limit for radar (i.e., >1 m) (D. Tamayo, personal communication). This would open up several new possibilities, though it would not solve the cratering apex–antapex conundrum.

5.2. The height of dark particle layers on the Galilean satellites

Our estimated maximum height for the dark particle layers produced on the Galilean satellites is shown in Fig. 13. Using the concept of NSR, the impacting material was evenly distributed across an outer layer of height h on each satellite. For >50 μm particles, h may have been up to 120–140 m for Callisto and 25–30 m for Ganymede. This corresponds to h ratio of 5 between Callisto and Ganymede. For Europa and Io, we predict h of 7–15 m and 7–8 m, respectively. If we use $D < 10$ μm particles, the h values for Callisto shrink to <30 m and the ratio of h values between the satellites moves to a factor between 1 and 3. Accordingly, we believe absolute values and ratios of h may help us constrain the nature of the initial irregular satellite population.

The characteristic particle size of dark material created in a collisional cascade that reaches the Galilean satellites is unknown. Ideally, spectral evidence could be used to constrain the size of

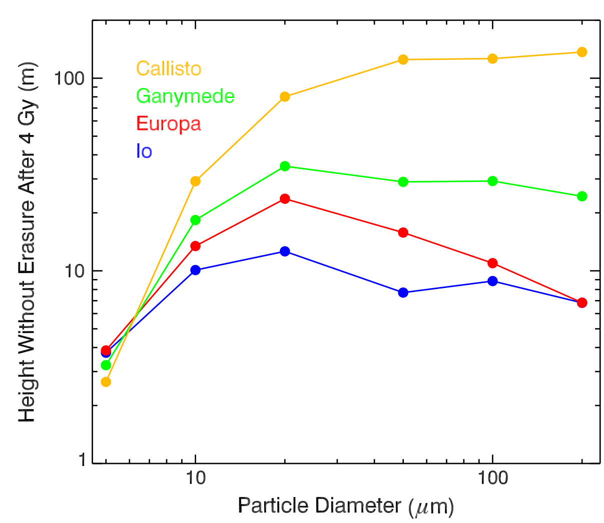

Fig. 13. The cumulative height of the dark particle layer produced on each Galilean satellites, assuming no erasure. It was obtained by combining the irregular satellite collision evolution results from Bottke et al. (2010) (see Fig. 6) with the irregular satellite particle accretion efficiency results determined in Fig. 10. The blue, red, green, and gold curves correspond to the height of a layer on Io, Europa, Ganymede, and Callisto, assuming they are perfect inert spheres and that the particles are evenly distributed across the surface. For $D > 50$ μm, the height of the layer on Callisto is a factor of five times larger than that on Ganymede. Note that most of this mass arrives within the first 40 My of the capture of the irregular satellites. Thus, we would expect the oldest terrains to be much darker than even modestly younger terrains.

the dark particles. For example, in modeling the reflectance spectrum of Callisto, Calvin and Clark (1991) got a best fit using various ice components and non-ice grains that were >50–100 μm in diameter. These sizes were needed to avoid suppressing the weaker ice bands. With that said, however, there are many processes that can effect surface spectra, including frost formation, space weathering, radiation, coatings of material derived from Io's volcanos, etc. As far as we can tell, there is no consensus on the particle sizes needed to match the spectra of these worlds.

An alternative way to attack this problem is by proxy. To this end, we offer the following chain of logic. By modeling the source populations and evolution of particles in the zodiacal cloud, Nesvorný et al. (2010) argued that most of the micrometeorites reaching Earth today must have come from disrupted Jupiter-family comets (JFCs). The source region of the JFCs is the scattered disk, a region in the transneptunian region (Duncan et al., 2004). Modeling work shows the scattered disk was created when the giant planets migrated through the primordial disk of comets within the context of the Nice model (Levison et al., 2008). Thus, the source population of the JFCs and the irregular satellites may be the same. We also know that antarctic micrometeorites are dominated by primitive carbonaceous chondrites similar to CI, CM, and CR meteorites (e.g., Genge et al., 2008). These compositions are consistent with the expected nature of comets.

If micrometeorite particles are a reasonable stand-in for irregular satellite particles, we can use the mass distribution of the former to approximate the latter. The best measurements of the latter come from micrometeorites found in Antarctic water wells (Taylor et al., 2000) as well as those inferred from impact craters on the Long Duration Exposure Facility (Love and Brownlee, 1995) and on the Genesis spacecraft (Love and Allton, 2006). All three yield a SFD with a steep power-law slope for $D > 200\ \mu m$ that breaks to a shallow power law slope for $D < 200\ \mu m$. This implies most of the mass in terrestrial micrometeorites comes from $D \sim 100$–$200\ \mu m$ particles. For our purposes, this size corresponds to the top end of our size range from our production runs.

5.2.1. Callisto and Ganymede

Here we assume most of the dark material from the irregular satellites arrives in the form of $D > 50\ \mu m$ particles. We will also assume that our Fig. 13 results are directly applicable to the oldest and darkest regions on Ganymede and Callisto. We believe this is reasonable because crater counts and chronology models suggest these terrains are perhaps ~4 Gy old, at least as old as the putative Late Heavy Bombardment of the inner Solar System (Gomes et al., 2005; Bottke et al., 2012; Morbidelli et al., 2012). Accordingly, these surfaces presumably contain a record of dark material from the time of irregular satellite capture around Jupiter. Taken together, our model predicts that (i) the h ratio between Callisto and Ganymede on the oldest, darkest terrains should be ~5, (ii) the h value at Callisto and Ganymede should be as much as 120–140 m and 25–30 m, respectively. Larger irregular satellite populations would naturally lead to larger values for h, though the ratio of particle depths between Callisto and Ganymede would remain the same.

Interestingly, these predictions may be a reasonable match to observations. Moore et al. (2004) report large mass wasting deposits on Callisto that are not found on any of the other Gallilean satellites. Some of these deposits, apparently derived from the crater walls within impact craters, reach depths of 90 m or so. Other observations of dark material on various Callisto features suggest that the height of dark material is of the order of 100 m or so. More broadly, these estimates fit with overall semi-buried appearance of Callisto features, which look like they are covered or at least mixed with dark material that is either sublimating out of the ice and/or is being gradually deposited (Figs. 2 and 5).

In contrast, the lag deposits in the most heavily cratered terrains on Ganymede (e.g., Galileo Regio) appear to be much smaller (Fig. 4). Prockter et al. (1998) report these regions, despite their expectations, do not look like comparable Callisto terrains. The height of the dark lag deposits on these terrains does not appear to exceed a few tens of meters (L. Prockter, personal communication). Thus, the ratio of the heights of the deepest deposits on Callisto vs. Ganymede, as well as the absolute abundances, appear broadly consistent with our estimates from (i) and (ii) above.

It is important to point out that the situation for many terrains is likely to be more complicated than what is described above. Surface processes such as mass wasting, sublimation, and tectonism are likely to strongly affect what we see, and the amount of dark material entrained in the crust and interior of these bodies cannot be easily determined from existing measurements. For that reason, we are careful in this paper to only compare our work to fairly broad trends and zeroth-order considerations. More involved calculations will require work that goes beyond the scope of this paper.

The striking color and albedo differences observed on Ganymede (Fig. 1) may also be a combination of particle deposition, dark lag deposits, and geologic processes that erase these deposits. Most of Ganymede can be characterized as relatively old regions of dark terrains and younger cross-cutting lanes of bright typically grooved terrain (Pappalardo et al., 2004). Our model results predict that factors like brightness and crater density should be correlated, with the brightness of the terrain potentially acting as a alternative clock to estimate surface age. Developing this chronology, however, requires a model of how much dark material is expected to be mixed into different geologic units. This topic is beyond the scope of this paper, though it may be interesting to examine this issue more closely in the future.

5.2.2. Europa

Nearly all of the dark material landing on the Galilean satellites lands shortly after the capture of the irregular satellites, when the populations are massive and collisional evolution is the most effective. The problem is that Europa and Io have very young surfaces. Crater counts on Europa suggest it is between 20 and 100 Ma (Bierhaus et al., 2009), while no craters have yet been found on Io. Thus, most of the putative dark material from Fig. 1 has been eliminated in some fashion.

To counter this, we decided to re-plot our results, with the height of the dark material on our worlds shown in Fig. 14 as a function of surface age. This time dependent flux of particles reaching the satellites was calculated by merging our impact efficiency results with the collisional modeling results described by Bottke et al. (2010). Recall that in Fig. 10, all of our particles were released simultaneously, while real irregular satellite particles are created by collisonal grinding. This means their starting time is measured from the moment their immediate precursor is disrupted very small enough fragments that they can be affected by P–R drag.

Once the irregular satellites grind themselves down to a low-mass state, the particle flux settles into a quasi-steady state that is occasionally modified by the stochastic disruption of an irregular satellite or by a large cratering event on a large irregular satellite. This explains why Fig. 14 shows step-function-like changes in the height of the dark material for surface ages <2 Gy.

Assuming Europa's surface is between 20 and 100 Ma, we predict that the dark material on top should be 0.05 to perhaps 0.5 cm thick. These values allow us to make some simplistic back of the envelope calculations. Spencer and Denk (2010) calculate the surface albedo of Europa using the equation:

$$A = A_d + (A_i - A_d)(1 - f)^q. \tag{21}$$

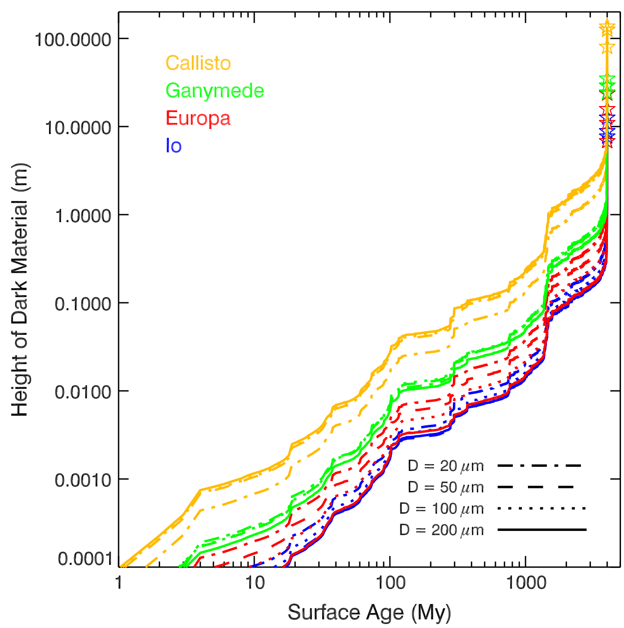

Fig. 14. The cumulative height of the dark particle layer expected on each Galilean satellite as a function of surface age. See Fig. 13 for computation details. The blue, red, green, and gold curves correspond to the height of a layer at a given surface age on Io, Europa, Ganymede, and Callisto. The different line styles correspond to our results for D = 20, 50, 100, and 200 μm particles. The open stars are the maximum height h of the dark particle layer found in each run, with the data taken from Fig. 13. These results show most dark particles arrive shortly after the capture of the irregular satellites. The maximum h values for the last 1 Gy are less than a few tens of cm. The step function nature of the curves corresponds to stochastic breakup events or large cratering events within the irregular satellite population, which can produce a surge of small particles.

Here A is the bolometric albedo of Europa (64%), A_d is the albedo of the dark particles (4%), A_i the albedo of pure ice, which we set to the same value of freshly fallen snow (80–90%), and f is the dark particle fraction. The value q is often set to 2 to account for the fact that a small amount of dark material may have a relatively large effect on albedo, but a linear albedo law of q = 1 may also be reasonable in situations where ice and dark material are spatially segregated on scales larger than the photon path length.

If we assume an end-member case where Europa's icy regolith contained no pre-existing lag deposit, and that q = 1 or 2, we estimate that an f value of 0.1–0.3 is needed to reproduce Europa's albedo. Accordingly, a dark material deposit of 0.05–0.5 cm over 20–100 Ma would suggest Europa's icy regolith should be between 0.17 and 5 cm thick. Interestingly, the average depth of the Europa's icy regolith is thought to be ~1 cm (Moore et al., 2004), roughly in the middle of our estimates. We caution, though, that this value should not be taken too seriously. There are other dark contaminants that may affect Europa's albedo (e.g., sulfur from Io's volcanoes), and Europa's albedo is probably better characterized as a combination of broad bright regions with dark patchy areas than an intimate mixture of bright and dark particles. Still, to zeroth order, this calculation may provide something of a consistency check for our work.

The fate of ~10 m of dark particles on ancient Europa is unknown. Presumably much of this material was mixed into the upper layers of these worlds by geologic and impact processes over the last 4 Gy. We suspect this debris is the source of the dark material that is exposed as a lag deposit after the ice sublimated (Fig. 3). Sublimation processes probably concentrate a small portion of this material in the faults, crevices or along the slopes of topographic features on Europa. The analogy here would perhaps be to a snowbank near the end of winter, which often contains enumerable dark particles and grit concentrated as the snow melts away.

It is also conceivable that geologic processes allowed some or perhaps most of this dark material to reach the putative subsurface ocean on Europa, thereby providing it with a source of organic compounds, including amino acids, and other contaminants. Antarctic micrometeorites, CM chondrites, and primitive meteorites like Tagish Lake consist of 2–6 wt.% carbon (Matrajt et al., 2003), though the abundance of organic carbon in some particles may reach 40% (Maurette et al., 1991). They may also have as much as 3–5% sulfur (Maurette et al., 1991, 2006).

The estimated volume of Europa ocean is thought to be 3×10^{18} m^3, provided it is 100 km thick and that it is covered by an icy shell that is 25 km thick. End-member ocean thickness estimates of 10–25 km, however, can also be fit to Europa's magnetic field data, depending on the assumed conductivity used for the ocean (Stevenson, 2003; Schilling et al., 2007). This would lower Europa's ocean volume to $3–7 \times 10^{17}$ m^3. The volume of a $h \sim$ 10–20 m thick blanket of dark material sitting on top of Europa's surface is ~$3–6 \times 10^{14}$ m^3. If all of it reached the subsurface ocean, and then stayed well-mixed within the ocean for billions of years, the ratio of dark material volume to ocean volume would range from 0.01% to 0.2%.

It has been suggested that keeping Europa's ocean in a liquid phase means it is probably a buoyant hypersaline brine that contains water and sulfates ($MgSO_4$). McKinnon and Zolensky (2003) compiled several estimates from the literature of the likely concentration of sulfates in Europa's ocean. They range from 0.002 wt.% all the way to 20 wt.% (their Table 1). Assuming an end-member case where the only contaminants in Europa's ocean are dark irregular satellite particles, we find solutions that can match the lowest sulfate fraction limits. Thus, the source of some of the key properties of Europa's ocean could conceivably come from irregular satellite particles.

5.3. Model caveats

The model presented here does not consider certain issues that should be examined in greater detail in the future. We discuss a few of these items below.

5.3.1. Particle survival

Our model assumes that particles reaching a particular size are essentially indestructible and survive all the way from the irregular to the Galilean satellite regions. This interval can last several hundreds of ky to several My, depending on particle size and the speed of P–R drag. It remains to be seen whether the collisional disruption lifetime of the particles in the ~10 μm to ~500 μm range are comparable to this timescale. If they were shorter, and the particles were disrupted prior to reaching the zone of regular satellites, we would need to take this effect into account to generate our dark particle depth heights. For example, one could imagine that some particles might be beaten down to sub-micron sizes during their orbital evolution phase. If so, their collision probabilities with the Galilean satellites would be smaller than predicted here.

On the other hand, the fact that our model results appear to match observations implies that the majority of the impacting particles are D > 50 μm as suggested here. If they were dominated by very small particles, we would not expect to see extensive dark terrains on the most ancient regions of Callisto and Ganymede.

5.3.2. Retention of irregular satellite debris on the Galilean satellites

We do not know what happens when these particles slam into a satellite's surface at high velocity. The energy of impact may heat the particle and some of the surface where it landed, with the vapor condensing back on the surface. It is unclear how this will affect the surface properties of the dust, the albedo of the surface, etc. On the other hand, observations of the dark material on

Saturn's moon Iapetus, which presumably comes from particles ejected from Phoebe, suggests that these issues may not play a critical role in our model interpretations. More work on these specific issues is needed. Additional discussion of these kinds of issues can be found in Bottke et al. (2010).

In terms of the fraction of solid material that stays on the Galilean satellites after a particle impact, we point out that Io, Europa, Ganymede, and Callisto all have large escape velocities >2 km s^{-1}, values that are comparable to that of our Moon. Gleaning insights from lunar impact simulations, we find that ~60% and ~15% of the mass of D > 1 km stone and pure water–ice projectiles, respectively, are retained on the Moon after an impact (Artemieva and Shuvalov, 2008). Because the impact velocities of irregular satellite debris with the Galilean satellites are comparable to or lower than those from Artemieva and Shuvalov (2008), and we are only concerned with the retention of the solid matter, not ice that can be vaporized, we believe it is reasonable to assume most of the dark material striking the Galilean satellites stays on the Galilean satellites.

5.3.3. Heliocentric sources of dark particles

We have yet to estimate the amount of dust accretion that Galilean satellite surfaces get from heliocentric sources. Using a back of the envelope calculation, we can estimate this contribution at Callisto. The flux of meteoroids from the interplanetary complex has been thoroughly examined by Divine (1993). His model provides $n \sim 5 \times 10^{-10}$ m^{-3} volumic density of $m \sim 10^{-9}$ g particles at Jupiter's heliocentric distance. Assuming a bulk density of ~2 g cm^{-3}, this roughly corresponds to a substantial influx of ~10 μm diameter particles.

The Divine (1993) flux onto the surface of Callisto with radius R can be estimated as $F \sim nR^2 \mathcal{F} v$, where $\mathcal{F}$ is the focusing factor due to Jupiter's gravity and v is the jovicentric orbital velocity of Callisto. We also choose to use particles with low encounter velocities with Jupiter ($v \sim 8$ km s^{-1}), allowing them to experience strong gravitational focusing effects (i.e., $\mathcal{F} \sim 60^2 \sim 1000$ and v dominated by the orbital motion of Callisto about the planet). Taking the integrated time $T \sim 4$ Gy, we estimate the total mass of particles accreted on Callisto from heliocentric orbits as $\sim FTm \sim 3 \times 10^{15}$ kg. This is roughly three orders of magnitude less material than that expected from the irregular satellites. Accordingly, we do not believe a heliocentric source particles strongly affects the work presented here.

With that said, we do not know what the dark particle flux was from heliocentric sources prior to 4 Ga. It was almost certainly much higher both before and during the scattering of the transplanetary disk of comets than it is today (Booth et al., 2009; Nesvorný et al., 2010). Even if lots of dust is produced in the transplanetary disk, however, it may not evolve down to 5 AU if the collisional disruption lifetime for the dark particles is shorter than the P–R drift timescale. We leave this intriguing issue for future work.

5.3.4. The role of indigenous dark material

It is possible that indigenous dark material (IDM) makes up a substantial fraction of what is seen on these worlds. Consider that the bulk ice-rock fraction increases outward from Jupiter among the Galilean satellites (e.g., Wong et al., 2008), and that tidal heating could supply a radially-dependent source of high albedos on Io and Europa. This would only leave the differences between Ganymede and Callisto as the main issue for external modifications, with a complex interplay taking place between the mix of IDM in the crust, the infall of dark debris, geologic processes, and impact regolith generation.

Still, this perhaps avoids the question of whether IDM is needed to explain observations. We note that it is difficult to attack this problem from the composition standpoint when so little is known about the properties of IDM vs. irregular satellite debris. The interested reader looking for insights is encouraged to examine papers on Saturn's irregular satellite Phoebe (Johnson and Lunine, 2005; Castillo-Rogez et al., 2012) and the irregular satellites (Jewitt and Haghighipour, 2007; Nicholson et al., 2008). Instead, we can probe this issue somewhat by examining what it would actually take for IDM to reproduce observations. We believe the evidence, though less than conclusive, may point toward a minimal IDM contribution.

Consider that for IDM to match observations, one would first need to keep a substantial fraction of IDM in the icy crusts and mantles of the Galilean satellites that have experienced partial or full differentiation. Assuming this took place, impacts into the crust/mantle would excavate ice laden with IDM, with the ice sublimating away to leave behind a dark surface lag deposit (i.e., as is often seen on a comet). Once the lag was deep enough, heating from the Sun via a thermal wave would no longer be able to reach the underlying material down to depth d. This would stop the sublimation process. Over time, therefore, the most heavily-cratered terrains might be expected to develop the deepest and most extensive lag deposits.

To dominate what we see, though, this scenario would need to overcome several issues:

- Fig. 1 shows that fresh impact craters on Ganymede and Callisto drill through a dark surface veneer and dig up relatively "clean" ice. As far as we know, a substantial IDM component has yet to be reported residing within the dredged up ice.
- If the fraction of IDM in the ice is modest, which would be consistent with the previous point, substantial ice sublimation would be needed to produce the observed dark material deposits. If this takes place, where does all of the sublimated ice go? On worlds like Iapetus, the ice goes to the poles or the trailing side (e.g., Spencer and Denk, 2010). Such bright ice deposits are not observed on Ganymede or Callisto.
- The skin depth of a lag deposit may be as low as a few cm in depth, at least if Pluto is any guide (M. Buie, personal communication). Once this depth is achieved, sublimation stops. This factor may make it difficult to build up a substantial IDM layer on the most ancient surfaces of Ganymede and Callisto.
- Similarly, once fresh ice is exposed, it would presumably sublimate until a sufficient lag deposit was created capable of stopping sublimation. If so, one might argue that this would make all non-active surfaces look largely the same, as they do on a comet. This would make it more difficult to explain why more heavily-cratered terrains on Ganymede have lower albedos.
- In this scenario, more impacts mean more opportunities to expose IDM-laden ice, which would sublimate into a lag deposit. Geologic processes, however, are also good at exposing fresh ice. This might suggest that ancient geologic features should produce some of the deeper and richer deposits of IDM. This is not obvious from images of the Galilean satellites.
- To produce a deep lag deposit, one presumably has to dredge up and expose lots of subsurface ice with IDM. On the ancient terrains of Ganymede and Callisto (e.g., Figs. 2, 4, and 5), however, we can still see underlying topography such as craters buried by dark material. Is it possible to create a thick, rich lag deposit of IDM from large quantities of sublimated ice yet still leave morphological features like craters intact enough that they can be easily noticed?
- In this scenario, one might expect the darkest regions on Ganymede to have smaller lag deposits via IDM than Callisto, since Ganymede is thought to be fully differentiated while Callisto may only be partially differentiated. Still, it is surprising something that the depth of the thickest lag deposits on Callisto are about five times that of Ganymede, exactly what our model results predicts from infalling irregular satellite debris.

We conclude from these items that the infall of dark material from the irregular satellites perhaps provides the easiest way to explain observations.

6. Conclusions

In this paper, we examined the fate of irregular satellite debris within the Jupiter system. This model took advantage of previous numerical modeling work (see Section 2) that suggested the irregular satellites were captured ~4 Ga during the final significant phase of giant planet migration as described by the Nice model (Tsiganis et al., 2005; Gomes et al., 2005; Nesvorný, 2011). A putative massive disk of comet-like objects located just outside the orbits of the giant planets was scattered and largely eliminated by giant planets roaming through this region. At the same time, the giant planets were having numerous close encounters with one another, which allowed some of the scattered but well-positioned comet-like objects to be captured around the giant planets by gravitational three-body reactions (Nesvorný et al., 2007). Ultimately, on the order of ~0.001 lunar masses of comet-like objects found themselves on orbits consistent with the known irregular satellites. From there, they experienced substantial collisional evolution, enough that most of the population was battered to bits (Bottke et al., 2010). These processes whittled the initial size distributions down to their current low-mass states. We argue the majority of the debris eventually took the form of small particles that were susceptible to Poynting–Robertson (P–R) drag.

We constructed a formalism that allowed us to model how Poynting–Robertson (P–R) drag should affect particles captured around generic giant planets (Section 3). We verified the work of others (e.g., Burns et al., 1979) that irregular satellite debris, in the form of small particles, is driven inward toward the central giant planet. Bodies initially captured in the high inclination Kozai resonance regions are lost over very short time scales, usually by striking the central planet or reaching orbits that are far beyond the planet's Hill sphere. Other particles initially placed on orbits similar to where the observed irregular satellites are found today drift inward slowly enough that they often have the opportunity to strike regular satellites orbiting close to the central planet.

We computed the accretion efficiency of irregular satellite particles evolving down to the Jupiter's regular satellites (Section 4). The particles themselves had $D = 5$, 10, 20, 50, 100, and 200 μm and bulk densities of 1 g cm^{-3}. Thousands of particles were assigned to each size and were given starting orbits with semimajor axes $a = 0.04$–0.18 AU, eccentricities $e = 0$–0.7, and isotropic inclinations. The particles were removed if they hit a satellite, Jupiter, or they reached beyond 0.6 AU from the planet. Fig. 10 shows our net accretion statistics. Nearly one-third of all our larger particles, with slower drift speeds than smaller ones, are swept up by Callisto, and over 40% ended up striking at least one the Galilean satellites. This means that particles avoiding Callisto often reach Ganymede, and to a lesser extent, Europa and Io.

These outcomes were intriguing because the oldest terrains on Callisto and Ganymede are the darkest, and they spectrally look like water ice contaminated by a blanket of dark, non-icy material with spectral properties similar to CI/CM meteorites (see Section 4). Coupling our satellite accretion results to a model of how the irregular satellite population may have collisionally evolved over time (Bottke et al., 2010), we obtained the following results:

- If the particles escaping the irregular satellite region were dominated by $D > 50$ μm, as suggested by several lines of evidence, we predict that 3–4 times and 20–40 as much dark material hit Callisto as hits Ganymede and Europa, respectively.
- Assuming that 0.0008 lunar masses was placed into quasi-stable orbits within the irregular satellite zone in the form of $D > 0.1$ km objects, and that most of this material was eventually ground down to $D > 50$ μm particles, we predict that Callisto should accrete a layer of coffee ground-like material five times deeper than the one on Ganymede, with most of this material arriving shortly after the capture of the irregular satellites ~4 Ga. We predict that the absolute height of the layers on Callisto and Ganymede should be $h \sim 120$–140 m and ~25–30 m, respectively. Both the ratio and the absolute values appear consistent with observations of dark lag material found on the most ancient terrains of Callisto and Ganymede. They could be even deeper if the assumed starting mass was larger, as suggested by some numerical simulations (Bottke et al., 2010).
- If Europa had an ancient surface like Callisto's, the height of its dark debris layer would be 10–20 m. Instead, cratering statistics suggest Europa's surface age is only 20–100 My. Over that interval, the height of the accumulated dark particle layer should be between 0.05 cm and 0.5 cm thick. Assuming this dark component was mixed into Europa's icy regolith, and that this is responsible for Europa's observed albedo of 64%, we predict Europa's regolith depth should be 0.17–2.5 cm thick. These values bracket the predicted regolith depth of ~1 cm (Moore et al., 2004).
- The missing dark material on Europa was likely removed by geologic processes. This probably provided it with an opportunity to become well-mixed within Europa's crust. We speculate that mechanism might provide a plausible source for the dark lag material observed on Europa, with the particles in low-lying regions concentrated by sublimation processes.
- It is also possible that the ancient dark debris was mixed deep enough into Europa's interior that it reached the putative subsurface ocean. Here it may act as a source for organic material and may increase the electric conductivity of the ocean itself, perhaps enough to help explain the observed magnetic field properties of Europa. Using an end-member model, where all of our predicted dark material reaches the subsurface ocean, we predict the concentration of dark material within Europa's ocean ranges between 0.01% and 0.2%.

We conclude with a prospectus of sorts. Nesvorný et al. (2007) predicted that Saturn, Uranus, and Neptune once had substantial irregular satellite populations of their own, while Bottke et al. (2010) showed these populations were likely decimated by collisonal evolution. This allowed Bottke et al. (2010) to argue that substantial layers of dark debris may have also found their way onto the moons of those systems as well, with the outermost moons of Saturn and the system of moons at Uranus potentially blanketed with dark debris. It will be interesting to explore in the future whether these predictions hold in these systems as well (e.g., Tamayo et al., 2011).

Acknowledgments

We thank Mark Buie, Carly Howett, Simone Marchi, Louise Prockter, and John Spencer for helpful discussions that improved this paper. We also thank referee Dan Tamayo and an anonymous referee for their constructive and highly useful comments. Research funds for William Bottke and David Nesvorný on this work were provided by NSF's Planetary Astronomy Program. The work of David Vokrouhlický was partially supported by research Grant 205/08/0064 of the Czech Grant Agency and the Research Program MSM0021620860 of the Czech Ministry of Education.

References

Agnor, C.B., Lin, D.N.C., 2012. On the migration of Jupiterand Saturn: Constraints from linear models of secular resonant coupling with the terrestrial planets. Astrophys. J. 745, 143 (20pp).

Alexander, C.M.O., Bowden, R., Fogel, M.L., Howard, K.T., Herd, C.D.K., Nittler, L.R., 2012. The provenances of asteroids, and their contributions to the volatile inventories of the terrestrial planets. Science 337, 721–723.
Artemieva, N.A., Shuvalov, V.V., 2008. Numerical simulation of high-velocity impact ejecta following falls of comets and asteroids onto the Moon. Solar Syst. Res. 42, 329–334.
Beaugé, C., Roig, F., Nesvorný, D., 2002. Effects of planetary migration on natural satellites of the outer planets. Icarus 158, 483–498.
Bell, J.F., 1984. Callisto: Jupiter's Iapetus? Lunar Planet. Sci. 15, 44–45 (abstracts).
Bell, J.F., Cruikshank, D.P., Gaffey, M.J., 1985. The composition and origin of the Iapetus dark material. Icarus 61, 192–207.
Bertotti, B., Farinella, P., Vokrouhlický, D., 2003. Physics of the Solar System. Kluwer Academic Publishers, New York.
Bierhaus, E.B., Zahnle, K., Chapman, C.R., 2009. Europa's crater distributions and surface ages. In: Pappalardo, R.T., McKinnon, W.B., Khurana, K.K. (Eds.), Europa. The University of Arizona Press, Tucson, pp. 161–180.
Bills, B.G., 2009. Planetary science: Tidal flows in satellite oceans. Nat. Geosci. 2, 13–14.
Booth, M., Wyatt, M.C., Morbidelli, A., Moro-Martín, A., Levison, H.F., 2009. The history of the Solar System's debris disc: Observable properties of the Kuiper belt. Mon. Not. R. Astron. Soc. 399, 385–398.
Bottke, W.F., Nolan, M.C., Greenberg, R., Kolvoord, R.A., 1994. Velocity distributions among colliding asteroids. Icarus 107, 255–268.
Bottke, W.F., Nesvorný, D., Vokrouhlický, D., Morbidelli, A., 2010. The irregular satellites: The most collisionally evolved populations in the Solar System. Astron. J. 139, 994–1014.
Bottke, W.F. et al., 2012. An Archaean heavy bombardment from a destabilized extension of the asteroid belt. Nature 485, 78–81.
Brozović, M., Jacobson, R.A., 2009. The orbits of the outer uranian satellites. Astron. J. 137, 3834–3842.
Buratti, B.J., 1991. Ganymede and Callisto – Surface textural dichotomies and photometric analysis. Icarus 92, 312–323.
Buratti, B.J., Mosher, J.A., 1991. Comparative global albedo and color maps of the uranian satellites. Icarus 90, 1–13.
Buratti, B.J., Mosher, J.A., 1995. The dark side of Iapetus: Additional evidence for an exogenous origin. Icarus 115, 219–227.
Buratti, B.J., Hicks, M.D., Tryka, K.A., Sittig, M.S., Newburn, R.L., 2002. High-resolution 0.33–0.92 μm spectra of Iapetus, Hyperion, Phoebe, Rhea, Dione, and D-type asteroids: How are they related? Icarus 155, 375–381.
Burns, J.A., Lamy, P.L., Soter, S., 1979. Radiation forces on small particles in the Solar System. Icarus 40, 1–48.
Burns, J.A., Hamilton, D.P., Mignard, F., Soter, S., 1996. The contamination of Iapetus by Phoebe dust. In: Gusafson, B.A.S., Soter, S. (Eds.), Physics, Chemistry, and Dynamics of Interplanetary Dust. ASP Conf. Ser. 104, San Francisco, pp. 179–182.
Burns, J.A., Hamilton, D.P., Showalter, M.R., 2001. Dusty rings and circumplanetary dust: Observations and simple physics. In: Grün, E., Gustafson, B.A.S., Dermott, S., Fechtig, H. (Eds.), Interplanetary Dust. Springer, Berlin, pp. 641–725.
Calvin, W.M., Clark, R.N., 1991. Modeling the reflectance spectrum of Callisto 0.25 to 4.1 microns. Icarus 89, 305–317.
Canup, R.M., Ward, W.R., 2009. Origin of Europa and the Galilean satellites. In: Pappalardo, R.T., McKinnon, W.B., Khurana, K.K. (Eds.), Europa. The University of Arizona Press, Tucson, pp. 59–83.
Carruba, V., Burns, J.A., Nicholson, P.D., Gladman, B.J., 2002. On the inclination distribution of the jovian irregular satellites. Icarus 158, 434–449.
Carruba, V., Burns, J.A., Nicholson, P.D., Gladman, B.J., 2003. Erratum to "on the inclination distribution of the jovian irregular satellites" [Icarus 158 (2002) 434–449]. Icarus 162, 230–231.
Castillo-Rogez, J.C., Johnson, T.V., Thomas, P.C., Choukroun, M., Matson, D.L., Lunine, J.I., 2012. Geophysical evolution of Saturn's satellite Phoebe, a large planetesimal in the outer Solar System. Icarus 219, 86–109.
Cruikshank, D.P. et al., 1983. The dark side of Iapetus. Icarus 53, 90–104.
Dalton, J.B., Cruikshank, D.P., Clark, R.N., 2012. Compositional analysis of Hyperion with the Cassini Visual and Infrared Mapping Spectrometer. Icarus 220, 752–776.
Divine, N., 1993. Five populations of interplanetary meteoroids. J. Geophys. Res. 98, 17029–17048.
Dones, L. et al., 2009. Icy satellites of Saturn: Impact cratering and age determination. In: Dougherty, M.K., Esposito, L.W., Krimigis, S.M. (Eds.), Saturn from Cassini–Huygens. Springer-Verlag, Dordrecht, pp. 613–635.
Duncan, M., Levison, H.F., Dones, L., 2004. Dynamical evolution of ecliptic comets. In: Festou, M., Keller, H.U., Weaver, H.A. (Eds.), Comets II. The University of Arizona Press, Tucson, pp. 193–204.
Ferraz-Mello, S., 1979. Dynamics of the Galilean Satellites. Universidade de Sao Paulo.
Genge, M.J., Engrand, C., Gounelle, M., Taylor, S., 2008. The classification of micrometeorites. Meteorit. Planet. Sci. 43, 497–515.
Gomes, R., Levison, H.F., Tsiganis, K., Morbidelli, A., 2005. Origin of the cataclysmic Late Heavy Bombardment period of the terrestrial planets. Nature 435, 466–469.
Hamilton, D.P., Krivov, A.V., 1996. Circumplanetary dust dynamics: Effects of solar gravity, radiation pressure, planetary oblateness, and electromagnetism. Icarus 123, 503–523.
Jacobson, R.A., 2000. The orbits of the outer jovian satellites. Astron. J. 120, 2679–2686.
Jacobson, R.A., 2002. The orientation of the pole of Jupiter. Bull. Am. Astron. Soc. 34, 936.
Jacobson, R.A., 2007. The orientation and precession of the pole of Saturn. Bull. Am. Astron. Soc. 39, 317.
Jacobson, R.A. et al., 2006. The gravity field of the saturnian system from satellite observations and spacecraft tracking data. Astron. J. 132, 2520–2526.
Jewitt, D., Haghighipour, N., 2007. Irregular satellites of the planets: Products of capture in the early Solar System. Annu. Rev. Astron. Astrophys. 45, 261–295.
Johnson, T.V., Lunine, J.I., 2005. Saturn's moon Phoebe as a captured body from the outer Solar System. Nature 435, 69–71.
Johnson, T.V., Soderblom, L.A., Mosher, J.A., Danielson, G.E., Cook, A.F., Kupperman, P., 1983. Global multispectral mosaics of the icy Galilean satellites. J. Geophys. Res. 88, 5789–5805.
Kennedy, G.M., Wyatt, M.C., 2011. Collisional evolution of irregular satellite swarms: Detectable dust around Solar System and extrasolar planets. Mon. Not. R. Astron. Soc. 412, 2137–2153.
Kivelson, M.G. et al., 1999. Europa and Callisto: Induced or intrinsic fields in a periodically varying plasma environment. J. Geophys. Res. 104, 4609–4626.
Kivelson, M.G., Khurana, K.K., Russell, C.T., Volwerk, M., Walker, R.J., Zimmer, C., 2000. Galileo magnetometer measurements: A stronger case for a subsurface ocean at Europa. Science 289, 1340–1343.
Kivelson, M.G., Khurana, K.K., Volwerk, M., 2002. The permanent and inductive magnetic moments of Ganymede. Icarus 157, 507–522.
Khurana, K.K. et al., 1998. Induced magnetic fields as evidence for subsurface oceans in Europa and Callisto. Nature 395, 777–780.
Laskar, J., 1988. Secular evolution of the Solar System over 10 million years. Astron. Astrophys. 198, 341–362.
Levison, H.F., Morbidelli, A., Van Laerhoven, C., Gomes, R., Tsiganis, K., 2008. Origin of the structure of the Kuiper belt during a dynamical instability in the orbits of Uranus and Neptune. Icarus 196, 258–273.
Levison, H.F., Bottke, W.F., Gounelle, M., Morbidelli, A., Nesvorný, D., Tsiganis, K., 2009. Contamination of the asteroid belt by primordial trans-neptunian objects. Nature 460, 364–366.
Lorenz, R.D. et al., 2008. Titan's rotation reveals an internal ocean and changing zonal winds. Science 319, 1649–1651.
Love, S.G., Allton, J.H., 2006. Micrometeoroid impact crater statistics at the boundary of Earth's gravitational sphere of influence. Icarus 184, 302–307.
Love, S.G., Brownlee, D.E., 1995. A direct measurement of the terrestrial mass accretion rate of cosmic dust. Science 262, 550–553.
Matrajt, G., Taylor, S., Flynn, G., Brownlee, D., Joswiak, D., 2003. A nuclear microprobe study of the distribution and concentration of carbon and nitrogen in Murchison and Tagish Lake meteorites, Antarctic micrometeorites, and IDPs: Implications for astrobiology. Meteorit. Planet. Sci. 38, 1585–1600.
Marchi, S., Bottke, W.F., Kring, D.A., Morbidelli, A., 2012. The onset of the lunar cataclysm as recorded in its ancient crater populations. Earth Planet. Sci. Lett. 325, 27–38.
Maurette, M. et al., 1991. A collection of diverse micrometeorites recovered from 100 tonnes of Antarctic blue ice. Nature 351, 44–47.
Maurette, M., Duprat, J., Engrand, C., Kurat, G., 2006. From Earth to Mars with micrometeorite volatiles. Adv. Space Res. 38, 701–708.
McCord, T.B. et al., 1998. Non-water-ice constituents in the surface material of the icy Galilean satellites from the Galileo near-infrared mapping spectrometer investigation. J. Geophys. Res. 103, 8603–8626.
McKinnon, W.B., Parmentier, E.M., 1986. Ganymede and Callisto. In: Burns, J.A., Matthews, M. (Eds.), Satellites. The University of Arizona Press, Tucson, pp. 718–763.
McKinnon, W.B., Zolensky, M.E., 2003. Sulfate content of Europa's ocean and shell: Evolutionary considerations and some geological and astrobiological implications. Astrobiology 3, 879–897.
Mignard, F., 1984. Effects of radiation forces on dust particles in planetary rings. In: Greenberg, R., Brahic, A. (Eds.), Planetary Rings. The University of Arizona Press, Tucson, pp. 333–366.
Milani, A., Nobili, A.M., Carpino, M., 1989. Dynamics of Pluto. Icarus 82, 200–217.
Minton, D.A., Malhotra, R., 2009. A record of planet migration in the main asteroid belt. Nature 457, 1109–1111.
Minton, D.A., Malhotra, R., 2011. Secular resonance sweeping of the main asteroid belt during planet migration. Astrophys. J. 732, 53 (12pp).
Mohit, P.S., Greenhagen, B.T., McKinnon, W.B., 2012. Polar wander on Ganymede: A possible solution to the apex–antapex cratering conundrum. LPI Contrib. 1649, 51–52.
Moore, J.M. et al., 2004. Callisto. In: Bagenal, F., Dowling, T., McKinnon, W.K. (Eds.), Jupiter, The Planet, Satellites and Magnetosphere. Cambridge University Press, Cambridge, pp. 397–426.
Morbidelli, A., Levison, H.F., Tsiganis, K., Gomes, R., 2005. Chaotic capture of Jupiter's Trojan asteroids in the early Solar System. Nature 435, 462–465.
Morbidelli, A., Levison, H.F., Bottke, W.F., Dones, L., Nesvorný, D., 2009a. Considerations on the magnitude distributions of the Kuiper belt and of the Jupiter Trojans. Icarus 202, 310–315.
Morbidelli, A., Bottke, W.F., Nesvorný, D., Levison, H.F., 2009b. Asteroids were born big. Icarus 204, 558–573.
Morbidelli, A., Brasser, R., Gomes, R., Levison, H.F., Tsiganis, K., 2010. Evidence from the asteroid belt for a violent past evolution of Jupiter's orbit. Astron. J. 140, 1391–1401.
Morbidelli, A., Marchi, S., Bottke, W.F., Kring, D.A., 2012. A sawtooth-like timeline for the first billion year of lunar bombardment. Earth Planet. Sci. Lett. 355, 144–151.

Morrison, D., Morrison, N.D., 1977. Photometry of the Gallilean satellites. In: Burns, J.A. (Ed.), Planetary satellites. The University of Arizona Press, Tucson, pp. 363–378.
Nesvorný, D., 2011. Young Solar System's fifth giant planet? Astrophys. J. 742, L22 (6 pp).
Nesvorný, D., Morbidelli, A., 2012. Statistical study of the early Solar System's instability with four, five, and six giant planets. Astron. J. 144, 117 (20 pp).
Nesvorný, D., Vokrouhlický, D., 2009. Chaotic capture of Neptune Trojans. Astron. J. 137, 5003–5011.
Nesvorný, D., Alvarellos, J.L.A., Dones, L., Levison, H.F., 2003. Orbital and collisional evolution of the irregular satellites. Astron. J. 126, 398–429.
Nesvorný, D., Beaugé, C., Dones, L., 2004. Collisional origin of families of irregular satellites. Astron. J. 127, 1768–1783.
Nesvorný, D., Vokrouhlický, D., Morbidelli, A., 2007. Capture of irregular satellites during planetary encounters. Astron. J. 133, 1962–1976.
Nesvorný, D., Jenniskens, P., Levison, H.F., Bottke, W.F., Vokrouhlický, D., Gounelle, M., 2010. Cometary origin of the zodiacal cloud and carbonaceous micrometeorites. Implications for hot debris disks. Astrophys. J. 713, 816–836.
Nicholson, P.D., Ćuk, M., Sheppard, S.S., Nesvorný, D., Johnson, T.V., 2008. Irregular satellites of the giant planets. In: Boehnhardt, H., Cruikshank, D.P., Morbidelli, A. (Eds.), The Solar System Beyond Neptune. The University of Arizona Press, Tucson, pp. 411–424.
Ogihara, M., Ida, S., 2012. N-body simulations of satellite formation around giant planets: Origin of orbital configuration of the Galilean moons. Astrophys. J. 753, 60 (17 pp).
Pappalardo, R.T. et al., 1999. Does Europa have a subsurface ocean? Evaluation of the geological evidence. J. Geophys. Res. 104, 24015–24056.
Pappalardo, R.T. et al., 2004. Geology of Ganymede. In: Bagenal, F., Dowling, T., McKinnon, W.K. (Eds.), Jupiter, The Planet, Satellites and Magnetosphere. Cambridge University Press, Cambridge, pp. 363–396.
Pollack, J.B., Witteborn, F.C., Erickson, E.F., Strecker, D.W., Baldwin, B.J., Bunch, T.E., 1978. Near-infrared spectra of the Galilean satellites – Observations and compositional implications. Icarus 36, 271–303.
Prockter, L.M. et al., 1998. Dark terrain on Ganymede: Geological mapping and interpretation of Galileo Regio at high resolution. Icarus 135, 317–344.
Peale, S.A., 1999. Origin and evolution of natural satellites. Annu. Rev. Astron. Astrophys. 37, 533–602.
Press, W.R., Teukolsky, S.A., Vetterling, W., Flannery, B.P., 2007. Numerical Recipes: The Art of Scientific Computing. Cambridge University Press, Cambridge.
Rhoden, A.R., Wurman, G., Huff, E.M., Manga, M., Hurford, T.A., 2012. Shell tectonics: A mechanical model for strike-slip displacement on Europa. Icarus 218, 297–307.
Schenk, P.M., Chapman, C.R., Zahnle, K., Moore, J.M., 2004. Ages and interiors: The cratering record of the Galilean satellites. In: Bagenal, F., Dowling, T., McKinnon, W.K. (Eds.), Jupiter, The Planet, Satellites and Magnetosphere. Cambridge University Press, Cambridge, pp. 427–456.
Schilling, N., Neubauer, F.M., Saur, J., 2007. Time-varying interaction of Europa with the jovian magnetosphere: Constraints on the conductivity of Europa's subsurface ocean. Icarus 192, 41–55.
Schubert, G., Anderson, J.D., Spohn, T., McKinnon, W.B., 2004. Interior composition, structure and dynamics of the Galilean satellites. In: Bagenal, F., Dowling, T., McKinnon, W.K. (Eds.), Jupiter, The Planet, Satellites and Magnetosphere. Cambridge University Press, Cambridge, pp. 281–306.
Seidelmann, P.K. et al., 2002. Report of the IAU/IAG working group on cartographic coordinates and rotational elements of the planets and satellites: 2000. Celest. Mech. Dynam. Astron. 82, 83–110.
Šidlichovský, M., Nesvorný, D., 1996. Frequency modified Fourier transform and its applications to asteroids. Celest. Mech. Dynam. Astron. 65, 137–148.
Soter, S., 1974. The brightness asymmetry of Iapetus. In: IAU Colloquium 28. Cornell University, New York (conference presentation).
Spencer, J.R., Denk, T., 2010. Formation of Iapetus' extreme albedo dichotomy by exogenically triggered thermal ice migration. Science 327, 432–435.
Stevenson, D.J., 2003. Planetary magnetic fields. Earth Planet. Sci. Lett. 208, 1–11.
Tamayo, D., Burns, J.A., Hamilton, D.P., Hedman, M.M., 2011. Finding the trigger to Iapetus' odd global albedo pattern: Dynamics of dust from Saturn's irregular satellites. Icarus 215, 260–278.
Tamayo, D., Burns, J.A., Hamilton, D.P., Nicholson, P.D., 2013. Dynamical Instabilities in High-Obliquity Systems. Astron. J. 145, 54 (12 pp).
Taylor, S., Lever, J.H., Harvey, R.P., 2000. Numbers, types, and compositions of an unbiased collection of cosmic spherules. Meteorit. Planet. Sci. 35, 651–666.
Tosi, F., Turrini, D., Coradini, A., Filacchione, G., 2010. Probing the origin of the dark material on Iapetus. Mon. Not. R. Astron. Soc. 403, 1113–1130.
Tsiganis, K., Gomes, R., Morbidelli, A., Levison, H.F., 2005. Origin of the orbital architecture of the giant planets of the Solar System. Nature 435, 459–461.
Tyler, R.H., 2008. Strong ocean tidal flow and heating on moons of the outer planets. Nature 456, 770–772.
Verbiscer, A.J., Skrutskie, M.F., Hamilton, D.P., 2009. Saturn's largest ring. Nature 461, 1098–1100.
Vokrouhlický, D., Nesvorný, D., Dones, L., Bottke, W.F., 2007. Thermal forces on planetary ring particles. Application to the main system of Saturn. Astron. Astrophys. 471, 717–730.
Vokrouhlický, D., Nesvorný, D., Levison, H.F., 2008. Irregular satellite capture by exchange reactions. Astron. J. 136, 1463–1476.
Vokrouhlický, D., Pokorný, P., Nesvorný, D., 2012. Öpik-type collision probability for high-inclination orbits. Icarus 219, 150–160.
Walsh, K.J., Morbidelli, A., Raymond, S.N., O'Brien, D.P., Mandell, A.M., 2011. A low mass for Mars from Jupiter's early gas-driven migration. Nature 475, 206–209.
Wong, M.H. et al., 2008. Oxygen and other volatiles in the giant planets and their satellites. In: MacPherson, G.J. (Ed.), Oxygen in the Solar System, vol. 241. Mineralogical Society of America, pp. 219–246.
Zahnle, K., Dones, L., Levison, H.F., 1998. Cratering rates on the Galilean satellites. Icarus 136, 202–222.
Zahnle, K., Schenk, P., Sobieszczyk, S., Dones, L., Levison, H.F., 2001. Differential cratering of synchronously rotating satellites by ecliptic comets. Icarus 153, 111–129.